Analysis of Fiber Clustering in Composite Materials Using High-Fidelity Multiscale Micromechanics

Brett A. Bednarcyk
Glenn Research Center, Cleveland, Ohio

Jacob Aboudi
Tel Aviv University, Ramat Aviv, Israel

Steven M. Arnold
Glenn Research Center, Cleveland, Ohio

NASA STI Program . . . in Profile

Since its founding, NASA has been dedicated to the advancement of aeronautics and space science. The NASA Scientific and Technical Information (STI) Program plays a key part in helping NASA maintain this important role.

The NASA STI Program operates under the auspices of the Agency Chief Information Officer. It collects, organizes, provides for archiving, and disseminates NASA's STI. The NASA STI Program provides access to the NASA Technical Report Server—Registered (NTRS Reg) and NASA Technical Report Server—Public (NTRS) thus providing one of the largest collections of aeronautical and space science STI in the world. Results are published in both non-NASA channels and by NASA in the NASA STI Report Series, which includes the following report types:

- TECHNICAL PUBLICATION. Reports of completed research or a major significant phase of research that present the results of NASA programs and include extensive data or theoretical analysis. Includes compilations of significant scientific and technical data and information deemed to be of continuing reference value. NASA counter-part of peer-reviewed formal professional papers, but has less stringent limitations on manuscript length and extent of graphic presentations.

- TECHNICAL MEMORANDUM. Scientific and technical findings that are preliminary or of specialized interest, e.g., "quick-release" reports, working papers, and bibliographies that contain minimal annotation. Does not contain extensive analysis.

- CONTRACTOR REPORT. Scientific and technical findings by NASA-sponsored contractors and grantees.

- CONFERENCE PUBLICATION. Collected papers from scientific and technical conferences, symposia, seminars, or other meetings sponsored or co-sponsored by NASA.

- SPECIAL PUBLICATION. Scientific, technical, or historical information from NASA programs, projects, and missions, often concerned with subjects having substantial public interest.

- TECHNICAL TRANSLATION. English-language translations of foreign scientific and technical material pertinent to NASA's mission.

For more information about the NASA STI program, see the following:

- Access the NASA STI program home page at http://www.sti.nasa.gov

- E-mail your question to help@sti.nasa.gov

- Fax your question to the NASA STI Information Desk at 757-864-6500

- Telephone the NASA STI Information Desk at 757-864-9658

- Write to:
  NASA STI Program
  Mail Stop 148
  NASA Langley Research Center
  Hampton, VA 23681-2199

Analysis of Fiber Clustering in Composite Materials Using High-Fidelity Multiscale Micromechanics

Brett A. Bednarcyk
Glenn Research Center, Cleveland, Ohio

Jacob Aboudi
Tel Aviv University, Ramat Aviv, Israel

Steven M. Arnold
Glenn Research Center, Cleveland, Ohio

National Aeronautics and
Space Administration

Glenn Research Center
Cleveland, Ohio 44135

Acknowledgments

The authors gratefully acknowledge Drs. Bradley A. Lerch and Pappu L.N. Murthy of NASA Glenn Research Center who provided the composite micrographs and the image pixel analysis results used herein.

Level of Review: This material has been technically reviewed by technical management.

Analysis of Fiber Clustering in Composite Materials Using High-Fidelity Multiscale Micromechanics

Brett A. Bednarcyk
National Aeronautics and Space Administration
Glenn Research Center
Cleveland, Ohio 44135

Jacob Aboudi
Tel Aviv University
Ramat Aviv 69978, Israel

Steven M. Arnold
National Aeronautics and Space Administration
Glenn Research Center
Cleveland, Ohio 44135

Abstract

A new multiscale micromechanical approach is developed for the prediction of the behavior of fiber reinforced composites in presence of fiber clustering. The developed method is based on a coupled two-scale implementation of the High-Fidelity Generalized Method of Cells theory, wherein both the local and global scales are represented using this micromechanical method. Concentration tensors and effective constitutive equations are established on both scales and linked to establish the required coupling, thus providing the local fields throughout the composite as well as the global properties and effective nonlinear response. Two nondimensional parameters, in conjunction with actual composite micrographs, are used to characterize the clustering of fibers in the composite. Based on the predicted local fields, initial yield and damage envelopes are generated for various clustering parameters for a polymer matrix composite with both carbon and glass fibers. Nonlinear epoxy matrix behavior is also considered, with results in the form of effective nonlinear response curves, with varying fiber clustering and for two sets of nonlinear matrix parameters.

Introduction

Clustering in composite materials refers to the aggregation of the constituents such that the composite does not exhibit uniform microstructural distribution. Composite microstructures are sensitive to the specific manufacturing processes utilized, and because the processing cannot be perfectly controlled, some degree of clustering will always be present. Clustering is more prevalent in composites with low fiber or inclusion volume fractions as there is more volume available in which one constituent may be segregated. In fact, in nanocomposites, whose volume fractions are typically very low, clustering is a dominant phenomenon, which strongly influences the properties and performance of the composite material (c.f., Shaffer and Windle (1999), Vigolo et al. (2000), Shi et al. (2004)).

Several investigators have presented methods to characterize the degree of clustering in composite materials (c.f., Guild and Summerscales (1993), Pyrz (1994), Scanlon et. al. (2003), Al-Ostaz et al. (2007), Vaughan and McCarthy (2010), Wilding and Fulwood (2011), Zangenberg et al. (2013)). In terms of modeling the effects of fiber clustering in composites, most investigations have been finite element based, as this approach can explicitly account for the composite microstructure. Examples include

Sorensen and Talreja (1993), Ghosh et al. (1997), Yang et al. (1997, 2000), Zeman and Sejnoha (2001), Wongsto and Li (2005), Melro et al. (2008), Abhilash et al. (2011), and Romanov et al. (2013). Additionally, the Generalized Method of Cells semi-analytical micromechanics theory has been employed to model random fiber distributions in continuous composites with a moving-window technique (Baxter and Graham (2000), Graham-Brady et al. (2003), Baxter et al. (2005), Acton and Graham-Brady (2010)).

In the present investigation, the triply-periodic High-Fidelity Generalized Method of Cells (HFGMC) (Aboudi et al., 2013) is first enhanced to enable coupled multiscale analysis, wherein both the local and global scales are synergistically linked. The HFGMC method determines the strain (or stress) concentration tensors, which are used to establish the macroscopic constitutive equations of the composite, and also to provide the local stress and strain fields throughout the composite. This enables the prediction of not only effective composite properties, but also the effective nonlinear response (due to local inelasticity and damage) in response to full multiaxial loading, as well as generation of initial yield and damage envelopes. The present multiscale HFGMC implementation considers an arbitrary number of local repeating unit cells (RUCs), which consist of the composite constituent materials (e.g., fiber and matrix). These local RUCs are then arranged in a global RUC, whose behavior represents that of the multiscale composite material. The scales are explicitly coupled so that any local nonlinearity (which can be predicted using the local fields) is homogenized and passed to the global scale analysis. The examples presented here utilize a two scale analysis, but the methodology could be generalized to admit an arbitrary number of scales, as has been done in the case of the Multiscale Generalized Method of Cells (Liu et al., 2011, Liu and Arnold, 2013; Bednarcyk et al., 2015).

Herein, the multiscale HFGMC approach is employed to examine the effects of fiber clustering in continuous fiber reinforced composites. A key aspect of the approach taken involves segregating the composite microstructure into two zones, A and B, see Figure 1. Each zone consists of a composite material with its own fiber volume fraction, thus, by varying the fiber volume fractions and the arrangement/size of zones A and B, fiber clustering can be represented. For example, if the fiber volume fraction in zone A is higher than that in zone B, the fiber-rich zone A represents a clustered region. Conversely, if the fiber volume fraction in zone B is higher than that in zone A, zone A will be a matrix-rich region as compared to zone B. It should be noted that the present method admits an arbitrary number of zones. The alternative single scale HFGMC or finite element approach to modeling fiber clustering would involve full discretization of the actual composite microstructure. Obviously, this implies the use of a very dense mesh with great potential for meshing issues in the local fiber-matrix regions. In contrast, the proposed multiscale HFGMC methodology captures the effects of fiber clustering through local scale fiber volume fraction variations. Thus coarse meshes can be used on both scales, avoiding these meshing concerns while balancing efficiency and fidelity. Further, while mean field approaches (e.g., Mori-Tanaka method) can predict reliable effective properties, the predicted mean fields do not capture the variations of the stress fields in the composite constituents, even in the case of uniform fiber distribution. Utilization of mean fields to predict initial yield envelopes was shown to be problematic via comparison to finite element micromechanics analyses by Pindera and Aboudi (1988) in the case of uniform fiber distribution. In the presence of fiber clustering, the matrix stress field variations are clearly important, thus motivating the use of a higher fidelity micromechanical approach such as HFGMC. It should be noted, however, that lower fidelity methods with better computational efficiency, such as the Generalized Method of Cells or the Mori-Tanaka Method, could be used to generate the results like those presented herein. The impact on these results of the better local fields given by HFGMC versus other methods has not been investigated.
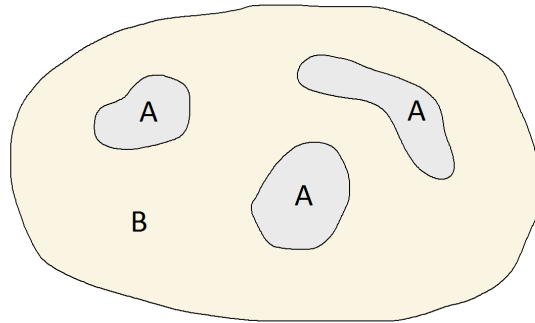
Figure 1.—Schematic drawing of a composite divided into two zones, A and B, which have different fiber volume fractions.

In the present investigation, actual micrographs from polymer matrix composites are used to determine these two zones within the composite RUC. The fiber clustering is characterized by two nondimensional parameters, one representing the volume fraction of zone A within the composite, and the other representing the fraction of the fibers that are located in zone A. Studies are performed by varying these parameters and observing their impact on the predicted initial global-scale yield and damage envelopes, as well as the nonlinear global stress-strain response. It should be noted that the availability of the concentration tensors in HFGMC enables straightforward and efficient generation of these initial envelopes. In contrast, the use of the standard finite element method would require repeated application of many loading combinations to trace out these surfaces.

The remainder of this paper is organized as follows. First, the multiscale HFGMC theory is presented for the generally triply-periodic case. Due to the possible nonlinearity of the constituent materials, an incremental (tangential) formulation is employed. The local and global concentration tensors and constitutive equations, as well as the coupling between them, are established. Next the methodology for determination of the initial yield and damage envelopes is described, followed by the method used to model fiber clustering. The Results and Discussion section details the processing of the composite micrographs to determine the analyzed composite RUCs. Results in the form of predicted effective properties, initial yield and damage envelopes, and macroscopic nonlinear stress-strain curves are presented for carbon/epoxy, glass/epoxy, and two different nonlinear representations of the epoxy matrix. The Conclusion section summarizes the paper and offers future research directions.

Multiscale High-Fidelity Generalized Method of Cells

In order to model the clustering of fibers in a composite material, the High-Fidelity Generalized Method of Cells (HFGMC) micromechanical model has been implemented in a two-scale framework. These two scales are referred to as global and local. The global scale represents a repeating unit cell of a periodic composite material, whose constituents are themselves periodic composite materials. Thus, the local scale represents the RUCs present within the global scale constituents, see Figure 2.
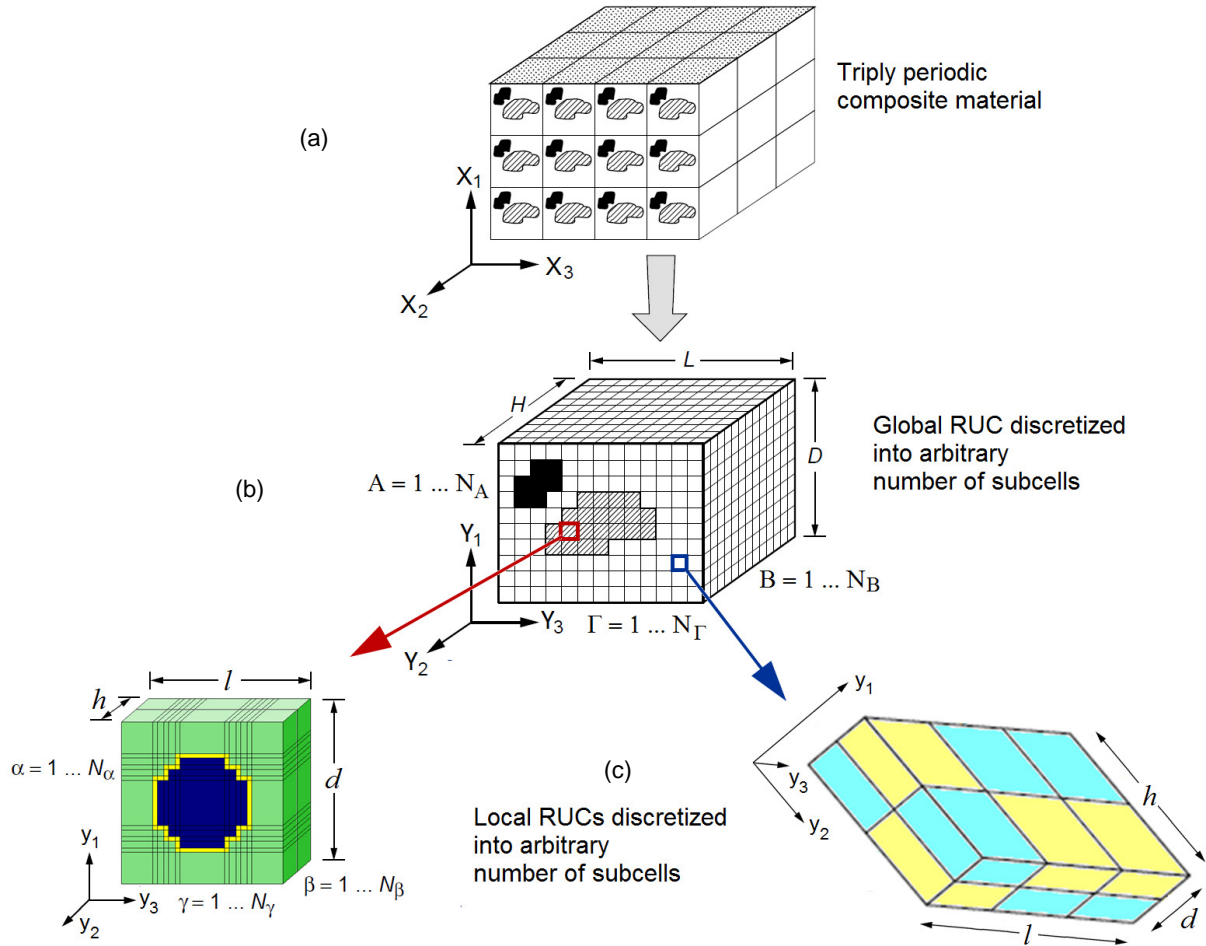
Figure 2.—(a) A multiphase composite with triply-periodic microstructure defined with respect to global coordinates (X_1, X_2, X_3). (b) Its repeating unit cell (RUC) is represented with respect to the coordinates (Y_1, Y_2, Y_3) and is divided into N_A, N_B, and N_Γ global-scale subcells, in the Y_1, Y_2, and Y_3 directions, respectively. (c) The materials within the global-scale subcells (ABΓ) are represented by local-scale RUCs, defined with respect to local coordinates (y_1, y_2, y_3), and is divided into N_α, N_β, and N_γ local-scale subcells.

Global Scale Analysis

The HFGMC theory, which has been fully described by Aboudi et al. (2013), considers a composite material with triply-periodic microstructure, Figure 2(a), wherein periodicity conditions are enforced in all three Cartesian coordinate directions. The global repeating unit cell (RUC), Figure 2(b), defined with respect to local coordinates (Y_1, Y_2, Y_3), is divided into N_A, N_B, and N_Γ global subcells in the Y_1, Y_2, and Y_3 directions, respectively. Each global subcell is labeled by the indices (ABΓ) with A = 1 ,…,N_A, B = 1,…,N_B and Γ = 1,…,N_Γ, and may contain a distinct homogeneous material or a composite material. The dimensions of the RUC are D, H, and L, whereas the dimensions of global subcell (ABΓ) in the Y_1, Y_2, and Y_3 directions are denoted by D_A, H_B, and L_Γ, respectively. A coordinate system $(\bar{Y}_2^{(A)}, \bar{Y}_2^{(B)}, \bar{Y}_3^{(\Gamma)})$ is introduced in each subcell whose origin is located at its center. The global subcell nonlinear elastic constitutive equation of the anisotropic material is given in an incremental form by,

$$\Delta\sigma_{ij}^{(\text{AB}\Gamma)} = C_{ijkl}^{(\text{AB}\Gamma)} \Delta\varepsilon_{kl}^{(\text{AB}\Gamma)} \tag{1}$$

where $\Delta\sigma_{ij}^{(\text{AB}\Gamma)}$, $\Delta\varepsilon_{kl}^{(\text{AB}\Gamma)}$, and $C_{ijkl}^{(\text{AB}\Gamma)}$ are the components of the stress increment, strain increment, and instantaneous (tangent) stiffness tensors of global subcell (ABΓ), respectively.

The basic assumption in HFGMC is that the increment of the displacement vector $\Delta U_i^{(\text{AB}\Gamma)}$ in each global subcell is represented as a second-order expansion in terms of its coordinates $(\overline{Y}_1^{(\text{A})}, \overline{Y}_2^{(\text{B})}, \overline{Y}_3^{(\Gamma)})$, as follows,

$$\begin{aligned}
\Delta U_i^{(\text{AB}\Gamma)} = {}& \Delta\overline{\varepsilon}_{ij}\ X_j + \Delta W_{i(000)}^{(\text{AB}\Gamma)} + \overline{Y}_1^{(\text{A})}\Delta W_{i(100)}^{(\text{AB}\Gamma)} + \overline{Y}_2^{(\text{B})}\Delta W_{i(010)}^{(\text{AB}\Gamma)} + \overline{Y}_3^{(\Gamma)}\Delta W_{i(001)}^{(\text{AB}\Gamma)} \\
& + \frac{1}{2}\left(3\overline{Y}_1^{(\text{A})2} - \frac{D_\text{A}^2}{4}\right)\Delta W_{i(200)}^{(\text{AB}\Gamma)} + \frac{1}{2}\left(3\overline{Y}_2^{(\text{B})2} - \frac{H_\text{B}^2}{4}\right)\Delta W_{i(020)}^{(\text{AB}\Gamma)} + \frac{1}{2}\left(3\overline{Y}_3^{(\Gamma)2} - \frac{L_\Gamma^2}{4}\right)\Delta W_{i(002)}^{(\text{AB}\Gamma)}
\end{aligned} \tag{2}$$

where $\Delta\overline{\varepsilon}_{ij}$ are the applied (external) average strain increments, and the unknown terms $\Delta W_{i(lmn)}^{(\text{AB}\Gamma)}$ must be determined from the fulfillment of the equilibrium conditions, the periodic boundary conditions, and the interfacial continuity conditions of displacements and tractions between global subcells. The periodic boundary conditions ensure that the increments of displacement and traction at opposite surfaces of the global RUC are identical. A principal ingredient in the HFGMC micromechanical analysis is that all these conditions are imposed in the average (integral) sense.

As a result of the imposition of these conditions, a linear system of algebraic equations is obtained, which can be represented in the following form:

$$\mathbf{K}\ \Delta\mathbf{V} = \Delta\mathbf{F} \tag{3}$$

where the matrix $\mathbf{K}$ contains information on the global geometry and instantaneous properties of the materials (or composites) within the individual subcells (ABΓ), and the displacement vector increment, $\Delta\mathbf{V}$, contains the unknown displacement coefficients $\Delta W_{i(lmn)}^{(\text{AB}\Gamma)}$, which appear on the right-hand side of Equation (2). The vector $\Delta\mathbf{F}$ contains information on the applied average strain increments $\Delta\overline{\varepsilon}_{ij}$. The solution of Equation (3) enables the establishment of the following localization relation which expresses the average strain increments $\Delta\overline{\varepsilon}_{ij}^{(\text{AB}\Gamma)}$ in the global subcell (ABΓ) to the externally applied average strain increments $\Delta\overline{\varepsilon}_{ij}$ in the form,

$$\Delta\overline{\varepsilon}_{ij}^{(\text{AB}\Gamma)} = A_{ijkl}^{(\text{AB}\Gamma)}\Delta\overline{\varepsilon}_{kl} \tag{4}$$

where $A_{ijkl}^{(\text{AB}\Gamma)}$ are the instantaneous global strain concentration tensor components, of the subcell (ABΓ).

The final form of the effective incremental constitutive law of the multiphase composite, which relates the average stress increments $\Delta\overline{\sigma}_{ij}$ and strain increments $\Delta\overline{\varepsilon}_{kl}$, is established as follows:

$$\Delta\bar{\sigma}_{ij} = C^*_{ijkl} \ \Delta\bar{\varepsilon}_{kl} \tag{5}$$

In this equation C^*_{ijkl} are components of the instantaneous effective global stiffness tensor, which are given by,

$$C^*_{ijkl} = \frac{1}{DHL} \sum_{A=1}^{N_A} \sum_{B=1}^{N_B} \sum_{\Gamma=1}^{N_\Gamma} D_A H_B L_\Gamma \ C^{(AB\Gamma)}_{ijpq} \ A^{(AB\Gamma)}_{pqkl} \tag{6}$$

Next, the components of the global instantaneous stress concentration tensor, $B^{(AB\Gamma)}_{ijkl}$, which relate the average stress increments in the global subcell, $\Delta\bar{\sigma}^{(AB\Gamma)}_{ij}$, to the average (global) stress increments, $\Delta\bar{\sigma}_{ij}$, are determined. By combining Equations (1) and (4), the subcell stresses are given by,

$$\Delta\bar{\sigma}^{(AB\Gamma)}_{ij} = C^{(AB\Gamma)}_{ijpq} A^{(AB\Gamma)}_{pqkl} \Delta\bar{\varepsilon}_{kl} \tag{7}$$

Then, using Equation (5), one obtains,

$$\Delta\bar{\sigma}^{(AB\Gamma)}_{ij} = B^{(AB\Gamma)}_{ijkl} \Delta\bar{\sigma}_{kl} \tag{8}$$

where,

$$B^{(AB\Gamma)}_{ijkl} = C^{(AB\Gamma)}_{ijpq} A^{(AB\Gamma)}_{pqrs} S^*_{rskl} \tag{9}$$

and S^*_{rskl} are components of the effective instantaneous global compliance tensor, which are the components of the inverse of the instantaneous global effective stiffness tensor, $\mathbf{C}^*$, see Equation (6).

Local Scale Analysis

As stated above and shown in Figure 2, the global subcells can be occupied by periodic composite materials, whose responses are determined by the micromechanical analysis of local RUCs. Therefore the global scale analysis subcell quantities are the RUC quantities in the local scale analysis. As such, the global subcell incremental constitutive equation (1) serves as the RUC constitutive equation for the local scale. The local subcell incremental nonlinear elastic constitutive equation is given by,

$$\Delta\sigma^{(AB\Gamma,\alpha\beta\gamma)}_{ij} = C^{(AB\Gamma,\alpha\beta\gamma)}_{ijkl} \Delta\varepsilon^{(AB\Gamma,\alpha\beta\gamma)}_{kl} \tag{10}$$

where the indices (ABΓ) indicate the global subcell and the indices ($\alpha\beta\gamma$) indicate the local subcell. As in the global scale analysis, the increment of the displacement vector $\Delta u^{(AB\Gamma,\alpha\beta\gamma)}_i$ in each local subcell is expanded into quadratic forms in terms the coordinates $(\bar{y}^{(AB\Gamma,\alpha)}_1, \bar{y}^{(AB\Gamma,\beta)}_2, \bar{y}^{(AB\Gamma,\gamma)}_3)$ centered in the local subcell, as follows,

$$\Delta u_i^{(ABΓ,\alpha\beta\gamma)} = \Delta\overline{\varepsilon}_{ij}^{(ABΓ)} \, \overline{Y}_j^{(p)} + \Delta w_{i(000)}^{(ABΓ,\alpha\beta\gamma)} + \overline{y}_1^{(ABΓ,\alpha)} \Delta w_{i(100)}^{(ABΓ,\alpha\beta\gamma)} + \overline{y}_2^{(ABΓ,\beta)} \Delta w_{i(010)}^{(ABΓ,\alpha\beta\gamma)}$$

$$+ \overline{y}_3^{(ABΓ,\gamma)} \Delta w_{i(001)}^{(ABΓ,\alpha\beta\gamma)} + \frac{1}{2}\left(3\overline{y}_1^{(ABΓ,\alpha)2} - \frac{d_{(ABΓ,\alpha)}^2}{4}\right) \Delta w_{i(200)}^{(ABΓ,\alpha\beta\gamma)}$$

$$+ \frac{1}{2}\left(3\overline{y}_2^{(ABΓ,\beta)2} - \frac{h_{(ABΓ,\beta)}^2}{4}\right) \Delta w_{i(020)}^{(ABΓ,\alpha\beta\gamma)} + \frac{1}{2}\left(3\overline{y}_3^{(ABΓ,\gamma)2} - \frac{l_{(ABΓ,\gamma)}^2}{4}\right) \Delta w_{i(002)}^{(ABΓ,\alpha\beta\gamma)} \tag{11}$$

where p = A,B,Γ for j = 1,2,3, respectively, and $d_{(ABΓ,\alpha)}$, $h_{(ABΓ,\beta)}$, and $l_{(ABΓ,\gamma)}$ are the dimensions of the local subcell ($\alpha\beta\gamma$) within the global subcell (ABΓ). The unknown local terms $\Delta w_{i(lmn)}^{(ABΓ,\alpha\beta\gamma)}$ are determined from the fulfillment of the equilibrium conditions, the periodic boundary conditions, and the interfacial continuity conditions of displacements and tractions between local subcells. Again, all of these conditions are imposed in the average sense.

The application of these conditions lead to the local system of linear algebraic equations, which can be written in the following form:

$$\mathbf{k} \, \Delta\mathbf{v} = \Delta\mathbf{f} \tag{12}$$

where the matrix $\mathbf{k}$ contains information on the local geometry and instantaneous properties of the materials within the individual subcells ($\alpha\beta\gamma$), and the local displacement vector increment, $\Delta\mathbf{v}$, contains the unknown local displacement coefficients $\Delta w_{i(lmn)}^{(ABΓ,\alpha\beta\gamma)}$, which appear on the right-hand side of Equation (11). The vector $\Delta\mathbf{f}$ contains information on the global subcell average strain increments $\Delta\overline{\varepsilon}_{ij}^{(ABΓ)}$. The solution of Equation (12) enables the establishment of the following localization relation which expresses the average local strain increments $\Delta\overline{\varepsilon}_{ij}^{(ABΓ,\alpha\beta\gamma)}$ in the local subcell ($\alpha\beta\gamma$) to the global subcell average strain increments $\Delta\overline{\varepsilon}_{kl}^{(ABΓ)}$ in the global subcell (ABΓ),

$$\Delta\overline{\varepsilon}_{ij}^{(ABΓ,\alpha\beta\gamma)} = A_{ijkl}^{(ABΓ,\alpha\beta\gamma)} \Delta\overline{\varepsilon}_{kl}^{(ABΓ)} \tag{13}$$

where $A_{ijkl}^{(ABΓ,\alpha\beta\gamma)}$ are the instantaneous strain concentration tensor components of the local subcell ($\alpha\beta\gamma$) within the global subcell (ABΓ). With the established $A_{ijkl}^{(ABΓ,\alpha\beta\gamma)}$, the local RUC effective instantaneous stiffness tensor, which corresponds to the global subcell effective instantaneous stiffness tensor, $C_{ijkl}^{(ABΓ)}$, in Equation (1), can be written as,

$$C_{ijkl}^{(ABΓ)} = \frac{1}{dhl}\sum_{\alpha=1}^{N_\alpha}\sum_{\beta=1}^{N_\beta}\sum_{\gamma=1}^{N_\gamma} d_{(ABΓ,\alpha)} \, h_{(ABΓ,\beta)} \, l_{(ABΓ,\gamma)} \, C_{ijpq}^{(ABΓ,\alpha\beta\gamma)} \, A_{pqkl}^{(ABΓ,\alpha\beta\gamma)} \tag{14}$$

As before, the components of the local instantaneous stress concentration tensor, $B_{ijkl}^{(ABΓ,\alpha\beta\gamma)}$, which relate the average stress increments in the local subcell, $\Delta\overline{\sigma}_{ij}^{(ABΓ,\alpha\beta\gamma)}$, to the global subcell average stress

increments, $\Delta\overline{\sigma}_{ij}^{(\text{AB}\Gamma)}$, are determined. By combining Equations (10) and (13), the local subcell stresses are given by,

$$\Delta\overline{\sigma}_{ij}^{(\text{AB}\Gamma,\alpha\beta\gamma)} = C_{ijpq}^{(\text{AB}\Gamma,\alpha\beta\gamma)} A_{pqkl}^{(\text{AB}\Gamma,\alpha\beta\gamma)} \Delta\overline{\varepsilon}_{kl}^{(\text{AB}\Gamma)} \tag{15}$$

Then, using Equation (1), one obtains,

$$\Delta\overline{\sigma}_{ij}^{(\text{AB}\Gamma,\alpha\beta\gamma)} = B_{ijkl}^{(\text{AB}\Gamma,\alpha\beta\gamma)} \Delta\overline{\sigma}_{kl}^{(\text{AB}\Gamma)} \tag{16}$$

where,

$$B_{ijkl}^{(\text{AB}\Gamma,\alpha\beta\gamma)} = C_{ijpq}^{(\text{AB}\Gamma,\alpha\beta\gamma)} A_{pqrs}^{(\text{AB}\Gamma,\alpha\beta\gamma)} S_{rskl}^{(\text{AB}\Gamma)} \tag{17}$$

and $S_{rskl}^{(\text{AB}\Gamma)}$ are components of the effective instantaneous global subcell compliance tensor, which are the components of the inverse of the instantaneous global subcell stiffness tensor, $\mathbf{C}^{(\text{AB}\Gamma)}$, see Equation (14).

Therefore, starting at the local scale, given the properties of the local-scale constituents (e.g., fiber and matrix) and their arrangement in the RUC, the local HFGMC provides the incremental system of algebraic equations (12), from which the instantaneous strain concentration tensor, $\mathbf{A}^{(\text{AB}\Gamma,\alpha\beta\gamma)}$, is determined. Equation (14) then provides the instantaneous effective stiffness tensor, $\mathbf{C}^{(\text{AB}\Gamma)}$, of each composite material on the local scale . At the global scale, these materials are located within the global subcells (ABΓ). Given the arrangement of these composite materials within the global RUC, the global HFGMC analysis provides the incremental system of algebraic equations (3), from which the global instantaneous strain concentration tensor, $\mathbf{A}^{(\text{AB}\Gamma)}$, is determined. Then, the effective instantaneous stiffness tensor of the entire multiscale material, $\mathbf{C}^{*}$, can be determined from Equation (6). Given external applied loading at the global scale, the stress and strain fields throughout the multiscale material (at both scales) can be obtained through the localization equations, Equations (4) and (8) for the global scale and Equations (13) and (16) for the local scale.

Initial Yield and Damage Envelopes—Methodology

In the present section, the methodology used to generate initial yield and damage envelopes within the multiscale HFGMC analysis is described. The yield surfaces are based on the traditional von Mises criteria, as defined by the equivalent stress in the local subcell, given by,

$$\overline{\sigma}_{eq}^{(\text{AB}\Gamma,\alpha\beta\gamma)} = \sqrt{\frac{3}{2}\hat{\sigma}_{ij}^{(\text{AB}\Gamma,\alpha\beta\gamma)}\hat{\sigma}_{ij}^{(\text{AB}\Gamma,\alpha\beta\gamma)}} = Y \tag{18}$$

where $\hat{\sigma}_{ij}^{(\text{AB}\Gamma,\alpha\beta\gamma)} = \overline{\sigma}_{ij}^{(\text{AB}\Gamma,\alpha\beta\gamma)} - \overline{\sigma}_{kk}^{(\text{AB}\Gamma,\alpha\beta\gamma)}\delta_{ij}\big/3$ are the subcell deviatoric stresses at the local scale, δ_{ij} is the Kronecker delta, and Y is the yield stress of the material in the local subcell in simple tension.

The damage initiation criterion, suggested by Lemaitre and Chaboche (1990), is used to express the critical strain energy release rate associated with loss of stiffness in brittle materials, which are typically highly dependent on the state of triaxial stress, $\sigma_h = \sigma_{kk}/3$. The average triaxiality function (Lemaitre, 2001) in the local subcell is given by,

$$\overline{R}_v^{(AB\Gamma,\alpha\beta\gamma)} = \frac{2}{3}\left(1 + \nu^{(AB\Gamma,\alpha\beta\gamma)}\right) + 3\left(1 - 2\nu^{(AB\Gamma,\alpha\beta\gamma)}\right)\left(\frac{\overline{\sigma}_h^{(AB\Gamma,\alpha\beta\gamma)}}{\overline{\sigma}_{eq}^{(AB\Gamma,\alpha\beta\gamma)}}\right)^2 \tag{19}$$

where $\nu^{(AB\Gamma,\alpha\beta\gamma)}$ is the Poisson's ratio of the isotropic local subcell and $\overline{\sigma}_h^{(AB\Gamma,\alpha\beta\gamma)}$ is the local subcell average hydrostatic pressure. The damage initiation criterion is then given by,

$$\overline{\sigma}_{eq}^{(AB\Gamma,\alpha\beta\gamma)}\sqrt{\overline{R}_v^{(AB\Gamma,\alpha\beta\gamma)}} = \sigma_{cr} \tag{20}$$

Where σ_{cr} is a material parameter that specifies the stress at which damage initiates for a uniaxial tensile test.

To generate a yield or damage initiation envelope in a given global scale stress plane, for example, $\overline{\sigma}_{11} - \overline{\sigma}_{22}$, the global stress component increments are expressed as,

$$\Delta\overline{\sigma}_{11} = R\sin\alpha \qquad\qquad \Delta\overline{\sigma}_{22} = R\cos\alpha \tag{21}$$

where R is the radial distance from the origin to a point located on the initial yield or damage surface in the $\overline{\sigma}_{11} - \overline{\sigma}_{22}$ stress plane and α is the corresponding polar angle. For a given α, the global subcell stress increments, $\Delta\sigma_{ij}^{(AB\Gamma)}$, are readily determined (in terms of R) by substituting Equation (21) into Equation (8),

$$\Delta\overline{\sigma}_{ij}^{(AB\Gamma)} = B_{ij11}^{(AB\Gamma)} R\sin\alpha + B_{ij22}^{(AB\Gamma)} R\cos\alpha \tag{22}$$

Substituting this equation into the local stress concentration equation (16),

$$\Delta\overline{\sigma}_{ij}^{(AB\Gamma,\alpha\beta\gamma)} = R\, B_{ijkl}^{(AB\Gamma,\alpha\beta\gamma)}\left(B_{kl11}^{(AB\Gamma)}\sin\alpha + B_{kl22}^{(AB\Gamma)}\cos\alpha\right) \tag{23}$$

Due to initial linearity, the yield or damage initiation envelope can be reached in just one increment, therefore, the local subcell stresses can be considered as equivalent to their increments. Then the local subcell stresses given by Equation (23), which are proportional to R, can be utilized in either initiation criterion, Equation (18) or (20), thus providing the value of R/Y or R/σ_{cr} corresponding to yield or damage initiation at the specified polar angle α.

Modeling of Fiber Clustering

Herein, the fiber clustering is modeled using two zones with two different volume fractions, which may be arranged arbitrarily. To this end, let the fiber reinforced composite material be composed of two distinct regions, zone A and zone B, which are distributed within the composite in an arbitrary manner, see Figure 1. Note that the number of zones is arbitrary, but herein we have chosen to use two to maximize the effect of clustering. Following Shi et al. (2004), the volume fractions of the fibers within each zone are denoted as c_f^A and c_f^B. Let V be the total volume of the composite and V^A the volume of zone A. In addition, let V_f and V_f^A be the total volume of fibers in the composite and within zone A, respectively. Consequently, the overall (average) volume fraction of the fibers in the composite is,

$$c_f = \frac{V_f}{V} \tag{24}$$

Further, the volume fraction of zone A within the composite is given by,

$$c_A = \frac{V^A}{V} \tag{25}$$

and the fraction of the fibers that are located in zone A is given by,

$$\zeta = \frac{V_f^A}{V_f} \tag{26}$$

These equations imply that within zone A, the fiber volume fraction is,

$$c_f^A = \frac{c_f}{c_A} \zeta \tag{27}$$

and within zone B, the fiber volume fraction is,

$$c_f^B = \frac{c_f(1-\zeta)}{1-c_A} \tag{28}$$

Note that, when $c_A = \zeta$, the fibers are uniformly distributed in the composite, and thus no clustering is present. When $c_A = 1$, the entire composite is occupied by zone A, whereas, when $c_A = 0$, the entire composite is occupied by zone B, with both of these conditions also representing no clustering. When $\zeta = 1$, all fibers are located in zone A, while zone B is pure matrix, which represents complete clustering. Likewise, when $\zeta = 0$, all fibers are located in zone B, while zone A is pure matrix, which also represents complete clustering. Therefore, for a given segregation of the composite into zones A and B, the degree of fiber clustering can be fully described by the values of c_A and ζ, both of which vary between 0 and 1.

For a given composite overall volume fraction, c_f, and a given volume fraction of zone A within the composite, c_A, the above equations impose limits on the variation ζ. In order for the fiber volume fractions of zones A and B, c_f^A and c_f^B, to remain less than 1, the maximum and minimum values of ζ are given by,

$$\zeta_{\min} = \frac{c_f + c_A - 1}{c_f}, \qquad \zeta_{\max} = \frac{c_A}{c_f} \tag{29}$$

Results and Discussion

The effect of fiber clustering could be investigated by arbitrarily selecting the global scale RUC and choosing various values of c_A and ζ. Here, on the other hand, a micrograph of the 0° ply within a continuous fiber carbon/epoxy composite, see Figure 3, has been used to provide a more realistic global scale RUC. The overall fiber volume fraction in this micrograph, determined via image pixel analysis is $c_f = 0.457$. To assist in dividing the composite into zones A and B, a 10 by 16 square grid was placed over the micrograph,

and the fiber volume fraction of each square was determined via image pixel analysis, see Table 1. Then, the grid squares could be distributed to zones A and B based on a cutoff value of the fiber volume fraction. That is, given a cutoff value for the fiber volume fraction (e.g., 0.55), all grid squares above this value were assigned to zone A, while the remaining squares were assigned to zone B. While the choice of cutoff value is arbitrary, herein three such values (0.55, 0.45, 0.38) were chosen to investigate the effect of fiber clustering, see Figure 4. Note that, once a cutoff value is chosen, the value of c_A is determined as the fraction of shaded (zone A) squares in Figure 4. The corresponding values of c_A are 0.26, 0.5, and 0.74, respectively. The value of ζ, on the other hand, must be specified as constrained by Equation (29). Thus, for $c_A = 0.26$, $0 \leq \zeta \leq 0.56$, for $c_A = 0.5$, $0 \leq \zeta \leq 1$, and for $c_A = 0.74$, $0.44 \leq \zeta \leq 1$. Once ζ was chosen, the fiber volume fractions within zones A and B were calculated from Equations (27) and (28).
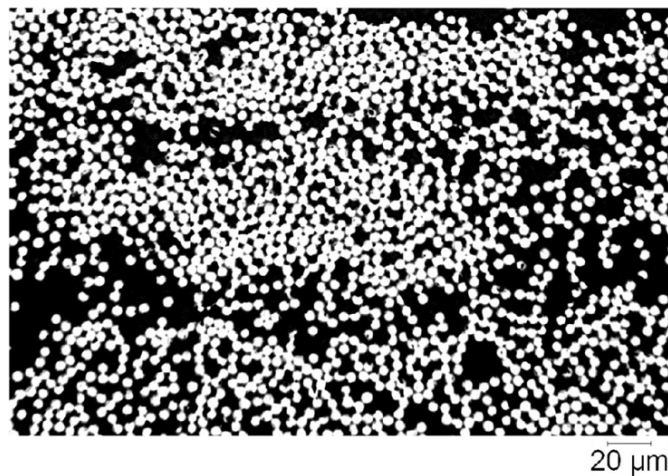
Figure 3.—Micrograph from the 0° ply in an IM7/MTM-45 carbon/epoxy composite. The overall fiber volume fraction, based on image pixel analysis, is 0.457.

TABLE 1.—FIBER VOLUME FRACTIONS OF THE 10 BY 16 SQUARE GRID THAT DIVIDES THE MICROGRAPH OF FIGURE 3. THE SHADED ENTRIES ARE THOSE WITH FIBER VOLUME FRACTIONS ABOVE 0.55, WHICH CORRESPOND TO THOSE SHADED IN FIGURE 4(A)

	1	2	3	4	5	6	7	8	9	10	11	12	13	14	15	16
1	0.648	0.507	0.715	0.701	0.609	0.466	0.562	0.485	0.573	0.449	0.411	0.431	0.328	0.577	0.271	0.267
2	0.509	0.512	0.435	0.506	0.577	0.575	0.706	0.604	0.662	0.714	0.592	0.645	0.638	0.650	0.382	0.417
3	0.447	0.473	0.357	0.465	0.518	0.483	0.559	0.469	0.548	0.537	0.447	0.387	0.428	0.482	0.450	0.446
4	0.380	0.490	0.554	0.252	0.487	0.381	0.537	0.611	0.586	0.532	0.404	0.362	0.516	0.314	0.373	0.454
5	0.375	0.515	0.612	0.627	0.674	0.602	0.559	0.573	0.573	0.573	0.652	0.468	0.486	0.305	0.362	0.271
6	0.278	0.384	0.366	0.404	0.515	0.692	0.699	0.652	0.654	0.566	0.570	0.642	0.424	0.310	0.234	0.299
7	0.188	0.182	0.253	0.110	0.419	0.438	0.347	0.359	0.421	0.598	0.489	0.409	0.306	0.342	0.200	0.317
8	0.068	0.341	0.507	0.373	0.294	0.507	0.395	0.242	0.359	0.341	0.385	0.386	0.436	0.369	0.464	0.506
9	0.298	0.414	0.382	0.386	0.385	0.465	0.596	0.520	0.455	0.565	0.462	0.374	0.361	0.440	0.406	0.385
10	0.446	0.482	0.389	0.410	0.418	0.442	0.416	0.472	0.451	0.439	0.330	0.500	0.330	0.534	0.597	0.462
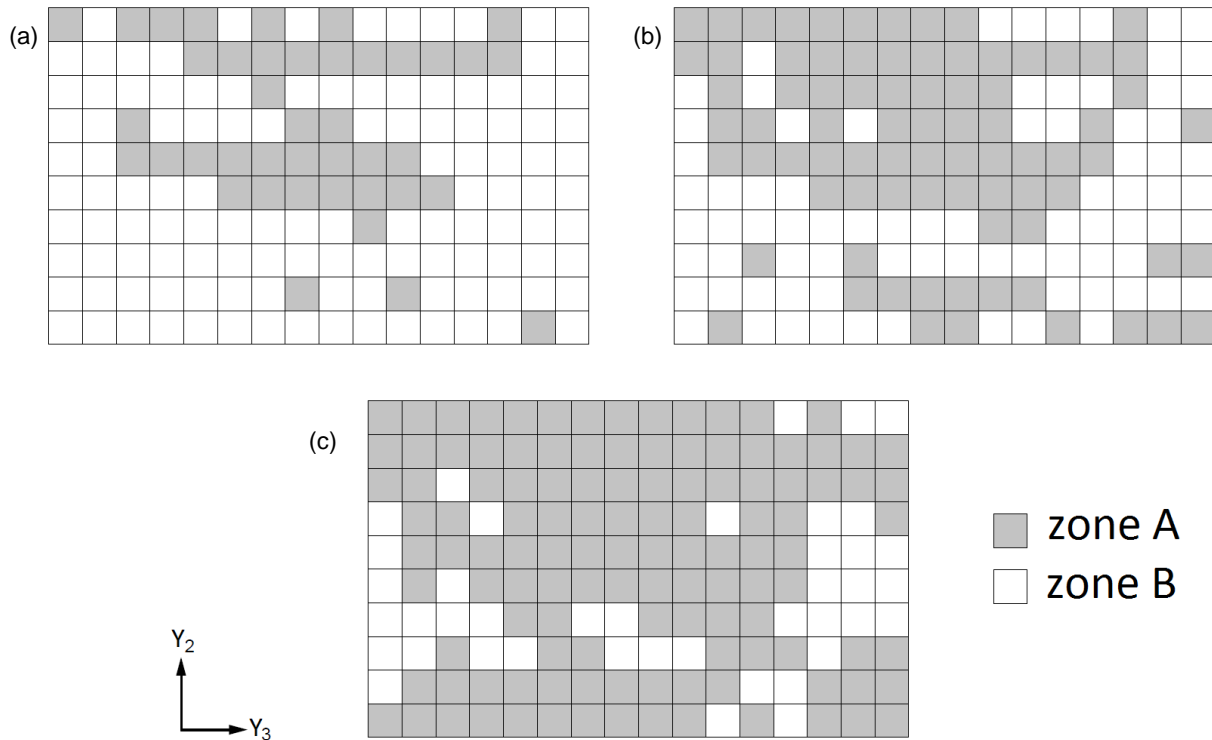
Figure 4.—Division of the micrograph (Figure 3) into zones A and B based on a cutoff value of the fiber volume fraction. (a) Cutoff fiber volume fraction = 0.55 and c_A = 0.26, (b) Cutoff fiber volume fraction = 0.45 and c_A = 0.5 (c) Cutoff fiber volume fraction = 0.38 and c_A = 0.74.

The microstructures shown in Figure 4 were employed as the global RUCs in the multiscale HFGMC analyses. At the local scale, 3 by 3 RUCs were employed to maximize efficiency, where the fiber volume fraction in zones A and B were adjusted to obtain the desired local fiber volume fractions, see Figure 5, Figure 6, and Figure 7. Note that square fiber packing was assumed at the local scale throughout this investigation. Table 2 provides a summary of the analysis cases considered associated with the micrograph in Figure 3.

The transversely isotropic carbon fiber properties used within the local scale RUCs are as follows: axial Young's modulus = 286 GPa, transverse Young's modulus = 12.4 GPa, axial shear modulus = 20 GPa, axial Poisson's ratio = 0.29, and transverse Poisson's ratio = 0.29. The isotropic epoxy matrix properties considered are: Young's modulus = 5.2 GPa and Poisson's ratio = 0.35. Throughout this study, the continuous fibers are oriented in the one-direction.
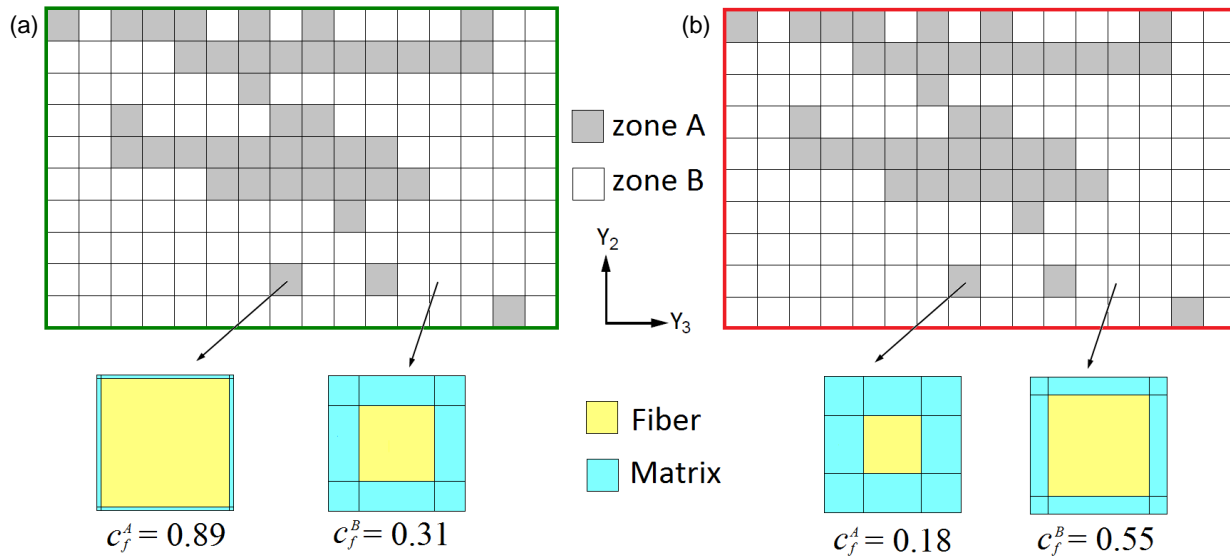
Figure 5.—Multiscale material distribution for $c_A = 0.26$ with (a) $\zeta = 0.5$ and (b) $\zeta = 0.1$.
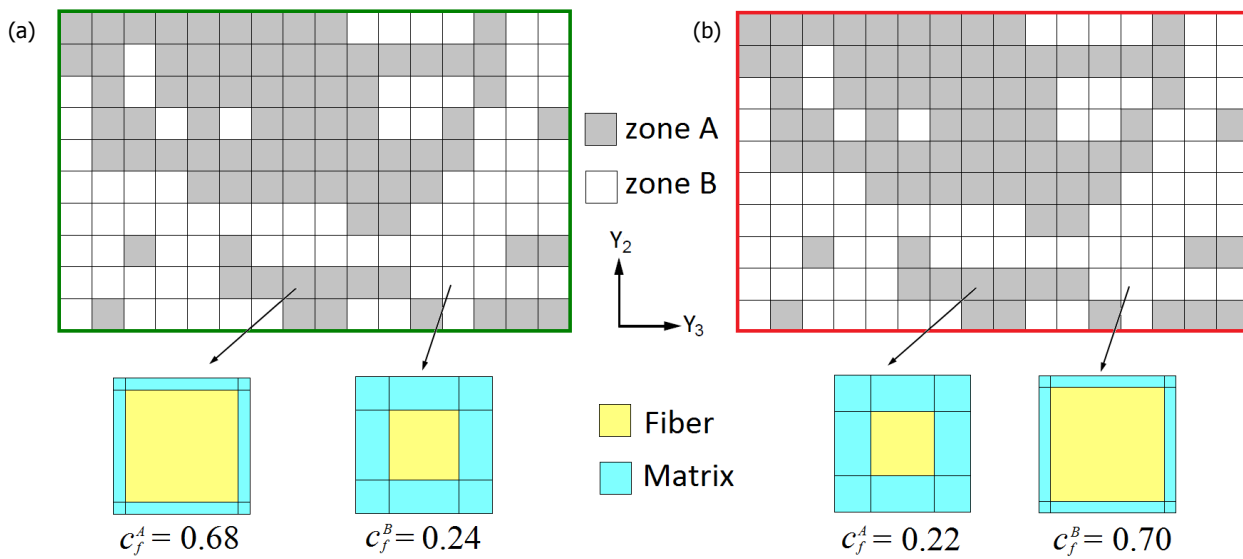
Figure 6.—Multiscale material distribution for $c_A = 0.5$ with (a) $\zeta = 0.74$ and (b) $\zeta = 0.24$.
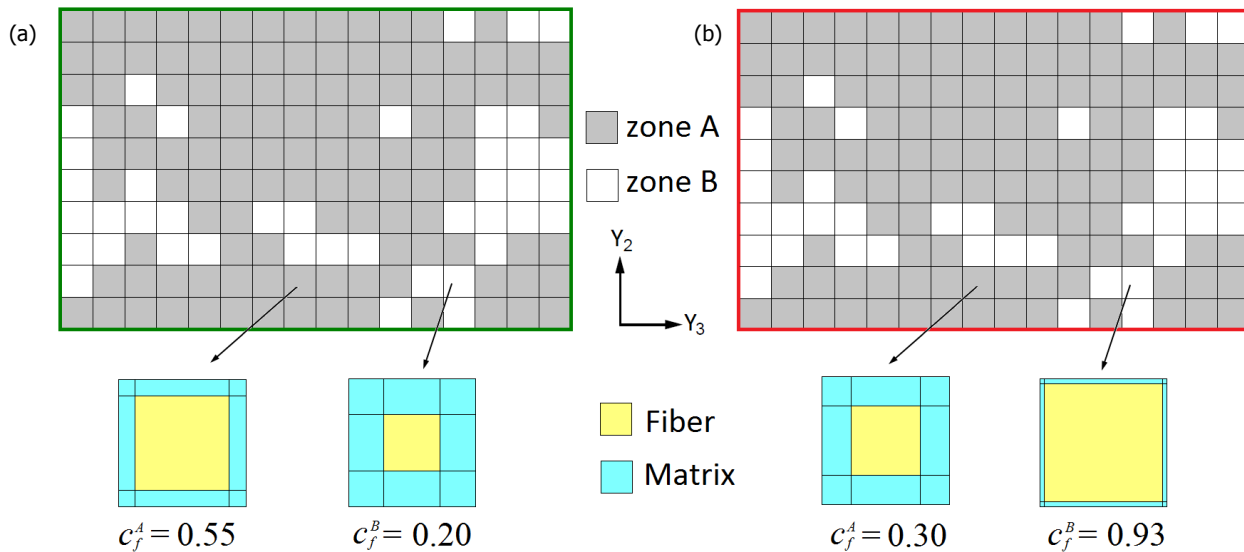
Figure 7.—Multiscale material distribution for $c_A = 0.74$ with (a) $\zeta = 0.89$ and (b) $\zeta = 0.48$.

$c_f^A = 0.55$ $c_f^B = 0.20$ $c_f^A = 0.30$ $c_f^B = 0.93$

TABLE 2.—SUMMARY OF THE FIBER CLUSTERING PARAMETER CASES CONSIDERED
FOR THE COMPOSITE MICROGRAPH SHOWN IN FIGURE 3

Cut off fiber volume fraction	c_A	ζ	c_f^A	c_f^B
Used to divide squares in micrograph into zones A and B	Volume fraction of zone A within the composite	Fraction of the fibers that are located in zone A	Fiber volume fraction within zone A	Fiber volume fraction within zone B
0.55	0.26	0.5	0.89	0.31
		0.1	0.18	0.55
0.45	0.5	0.74	0.68	0.24
		0.24	0.22	0.7
0.38	0.74	0.89	0.55	0.2
		0.48	0.3	0.93

Effective Elastic Properties

The effect of fiber clustering on the effective properties can be extracted from the effective stiffness tensor, $\mathbf{C}^*$. In fact, the determination of $\mathbf{C}^*$ does not require the coupled multiscale approach employed herein. Rather, by homogenizing zones A and B independently, and then employing the resulting stiffness tensors in a separate, uncoupled, homogenization procedure, $\mathbf{C}^*$ could also be determined. Here, however, the fully coupled approach was used. It is emphasized that the initial yield and damage envelopes presented in the next section, based on constituent properties, necessitate the use of a coupled multiscale approach as the fields at the local scale are required.

Figure 5 shows the microstructural details of the case where $c_A = 0.26$. This figure illustrates the global and local RUC geometries used to consider the cases of $\zeta = 0.5$ and $\zeta = 0.1$. For $\zeta = 0.5$, one half of the fibers are located in zone A, which is considerably smaller than zone B. Therefore, the volume fraction in zone A is quite high ($c_f^A = 0.89$), whereas $c_f^B = 0.31$ (maintaining the overall $c_f = 0.457$). In

contrast, for $\zeta = 0.1$, only 10 percent of the fibers are located in zone A. Thus the fiber volume fractions of zone A and zone B are reversed, with $c_f^A = 0.18$, whereas $c_f^B = 0.55$. Both cases represent deviations from uniform distribution of fibers in the composite; i.e., clustering. The additional cases where $c_A = 0.5$ and 0.74 are depicted in Figure 6 and Figure 7.

Figure 8 shows the normalized effective axial and transverse (in both directions) Young's moduli (E_{11}, E_{22}, and E_{33}) and the normalized effective axial shear modulus (G_{12}) of the composite for different values of c_A and ζ. For each of the three cases in Figure 4, two values of the parameter ζ, which indicates the fraction of fibers located in zone A, are considered: one which provides higher fiber volume fraction in zone A and the other that provides higher fiber volume fraction in zone B. The results are normalized by the uniform fiber distribution case, which can be obtained by setting $c_A = \zeta$. Clearly, the impact of fiber clustering on the effective properties of the composite is minor. The maximum variation, which occurred for G_{12}, is approximately 6 percent versus the uniform fiber distribution case. This validates the traditional approach of predicting composite effective elastic properties by considering a uniform fiber distribution. It is interesting to note that, while clustering resulted in slight reductions in the effective transverse Young's moduli, E_{22} and E_{33}, it resulted in a slight increase in the effective axial shear modulus, G_{12}. Of course, the comparison is made to the case of uniform fiber distribution, which herein assumes square fiber packing.

Initial Yield and Damage Envelopes

In this section, the initial yield and damage envelopes are presented for several global scale stress planes while varying the fiber clustering. A parametric study is performed by varying the value of c_A as shown in Figure 4. As in the case of the effective elastic properties above, for each of the three cases in Figure 4, two values of the parameter ζ are considered: one which provides higher fiber volume fraction in zone A and the other that provides higher fiber volume fraction in zone B. Details are shown in Figure 5 to Figure 7. Also shown in the initial envelopes for comparison is corresponding case with uniform fiber distribution.
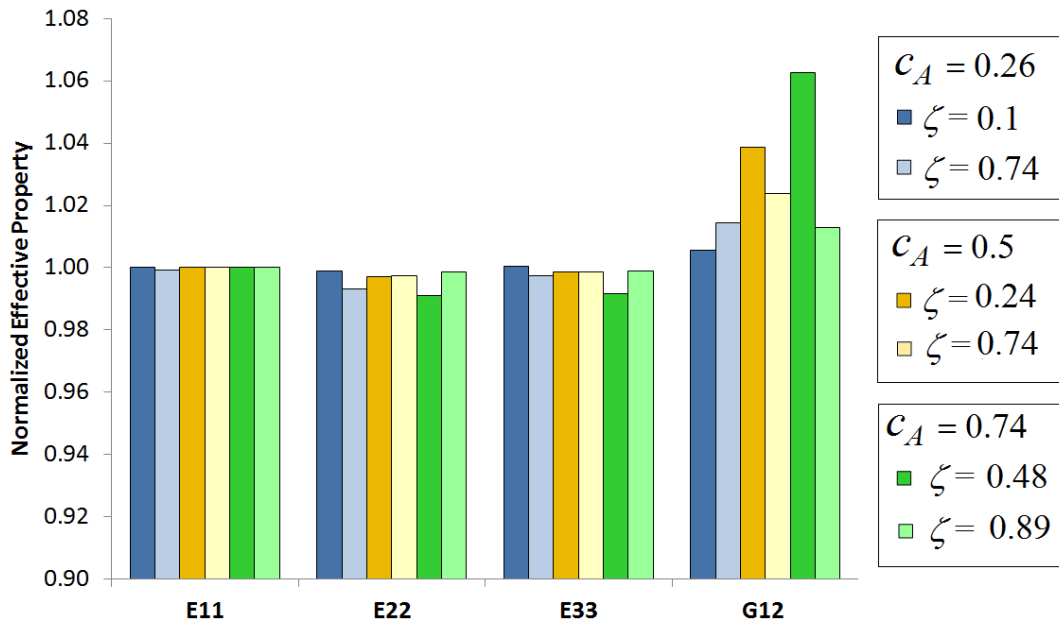
Figure 8.—The effect of fiber clustering on the normalized effective elastic properties of the composite.

Figure 9 shows the initial yield and damage envelopes for $c_A = 0.26$ for uniform fiber distribution and clustering with $\zeta = 0.5$ and $\zeta = 0.1$. Note that the stress magnitudes are normalized with respect to the yield stress (Y_m) or critical damage stress (σ_{cr-m}) of the isotropic matrix in simple tension, see Equations (18) and (20). Further, the predictions of the initial envelopes are based on the yielding and damage of the first matrix subcell within the local scale RUCs. That is, the fiber is not permitted to yield or damage.

Comparing the initial yield envelopes with their corresponding initial damage envelopes, the effect of the inclusion of hydrostatic stress in the damage criterion is seen as the damage envelopes are in all cases smaller than the corresponding yield envelopes. This is particularly true in the σ_{22}-σ_{33} envelopes, wherein the global hydrostatic stress is maximized in quadrants I and III. Clearly, the effect of clustering is significant since the envelopes that include this effect are always inside the envelopes associated with uniform fiber distribution. It should be emphasized that these initiation envelopes may or may not be representative of composite ultimate strength. In brittle systems (e.g., ceramic matrix composites), however, they would be expected to be more representative of final failure. In addition, the $\zeta = 0.5$ envelopes are always inside the $\zeta = 0.1$ envelopes. This is likely caused by the very high fiber volume fraction of zone A ($c_f^A = 0.89$) in the case of $\zeta = 0.5$, which results in high local scale stress concentrations in the matrix.

It is interesting that initiation of yielding and damage may occur in either zone A or zone B at each point on each envelope, thus diamond symbols are included in Figure 9 to indicate the portions of each envelope where initiation occurred in zone A. Transitions between zone A initiation and zone B initiation occur in many of the presented envelopes, while some exhibit initiation only in zone B (solid lines with no symbols). Obviously, for the case of uniform fiber distribution, there is no distinction between zones A and B, thus such transitions are not applicable.

Examining the initial σ_{11}-σ_{22} yield and damage envelopes reveals that, as expected, the effect of the continuous fibers is dominant as there is approximately a 25:1 difference in initiation stress for pure σ_{11} versus pure σ_{22}. Also, the effect of clustering is negligible under pure axial loading. Also of note is the fact that the damage initiation always occurs in zone B irrespective of the value of ζ. In contrast, this parameter has a pronounced effect on the initiation location in the case of yielding.

Considering biaxial loading in the transverse directions (σ_{33}-σ_{22}), the effect of the fiber is minimized. Here, all of the envelopes are nearly symmetric, and the locations of the transitions between zone A and zone B initiation are qualitatively similar between the yield and damage surfaces.
The effect of clustering is most evident in the initial σ_{12}-σ_{22} yield and damage envelopes. The predicted envelopes appear to be concentric ellipses whose semimajor axes are dictated by the clustering. For $\zeta = 0.5$, the yield and damage envelopes exhibit similar transitions from zone A to zone B initiation. However, for $\zeta = 0.1$, such transitions are present only in the yield envelope. It is interesting to note that while the initial yield and damage points under pure axial shear (which are based on the local fields) are reduced by the presence of clustering, the effective axial shear moduli shown in Figure 8 (which are based on the two-scale homogenized stiffness tensor) show an increase due to clustering.

The microstructural details in the case of $c_A = 0.5$ and $\zeta = 0.74$ and $\zeta = 0.24$ are shown in Figure 6. The corresponding initial yield and damage envelopes are shown in Figure 10. Similarly, for the case of $c_A = 0.74$ and $\zeta = 0.89$ and $\zeta = 0.48$, the microstructural details are given in Figure 7, and the associated initial envelopes are given in Figure 11. A comparison of Figure 9, Figure 10, and Figure 11, in which the volume fraction of zone A, c_A, increases from 0.26 to 0.5 to 0.74, reveals that, while all representations of clustering provide smaller yield envelopes compared to the uniform case, the ordering of high ζ and low ζ envelopes switches. In Figure 9, the higher ζ envelopes are smallest, in Figure 10 the higher and lower ζ
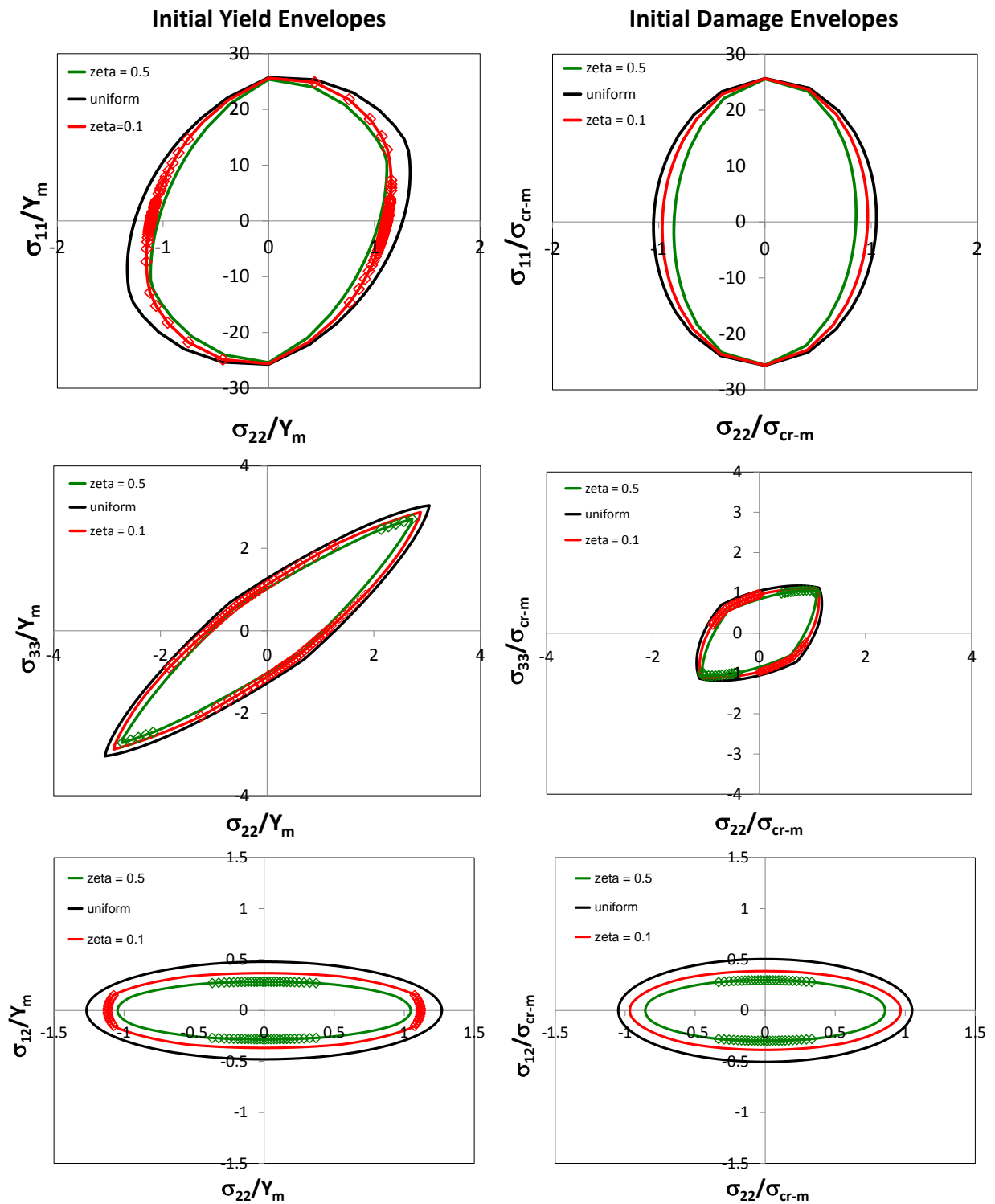
Figure 9.—Initial yield and damage envelopes for c_A = 0.26 associated with Figure 5. The symbols on certain envelopes indicate yield/damage initiation within zone A, whereas, when no symbol is present, failure initiated in zone B.
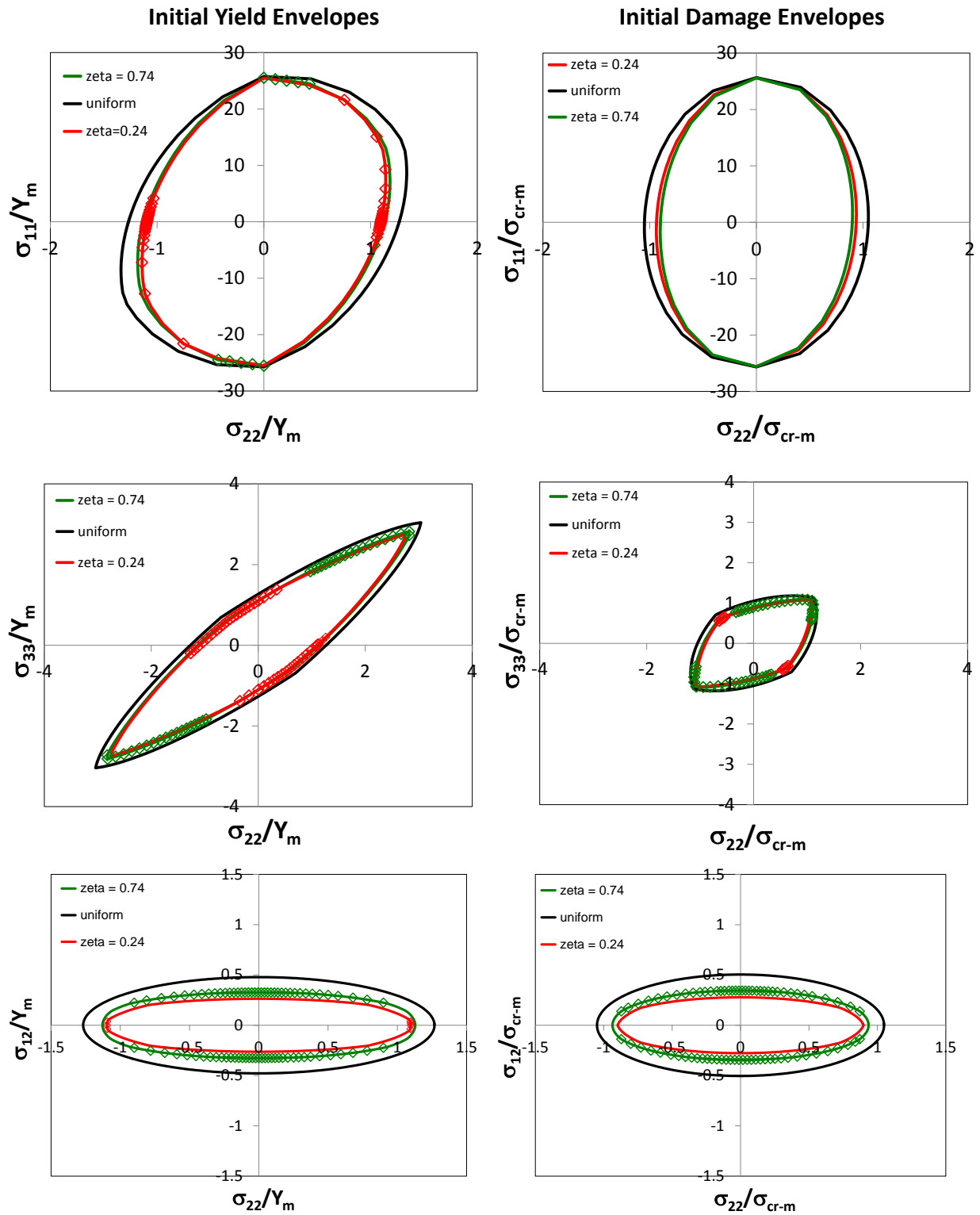
Figure 10.—Initial yield and damage envelopes for $c_A = 0.5$ associated with Figure 6. The symbols on certain envelopes indicate yield/damage initiation within zone A, whereas, when no symbol is present, failure initiated in zone B.
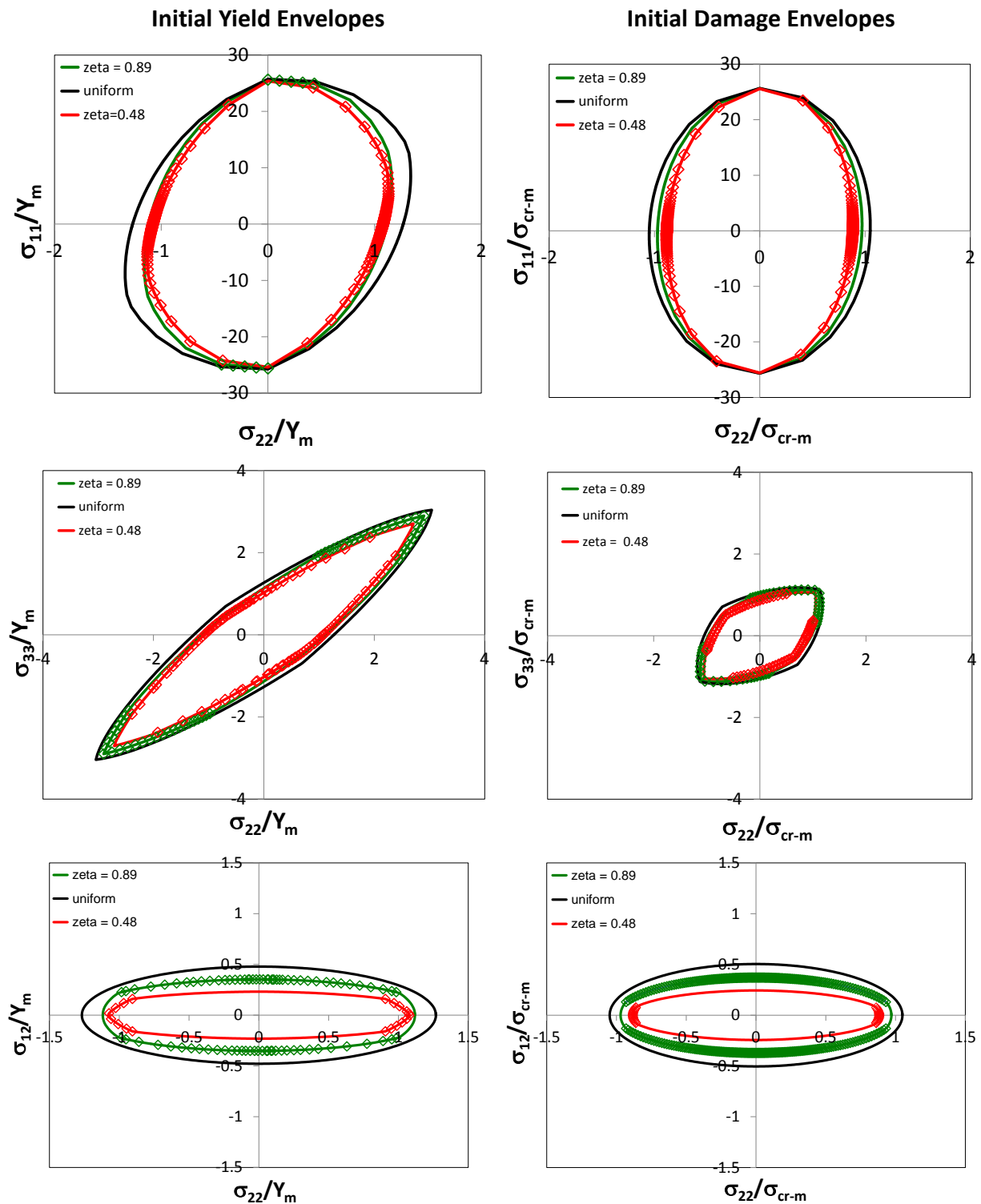
Figure 11.—Initial yield and damage envelopes for $c_A = 0.74$ associated with Figure 7. The symbols on certain envelopes indicate yield/damage initiation within zone A, whereas, when no symbol is present, failure initiated in zone B. Note that in the σ_{11}-σ_{22} envelopes for $\zeta = 0.48$, under pure σ_{11} loading, yield and damage initiated in zone B (these two points on these envelopes have no symbol).

envelopes are very close, and in Figure 11, the lower ζ envelopes are smallest. This observation is reasonable since the smallest envelopes are always associated with the higher local fiber volume fraction being located in the zone with the lower volume fraction within the global RUC. This situation represents the greater degree of fiber clustering and leads to higher stress concentrations in the composite, and thus contracted initial envelopes. It should be noted that, as before, the transitions of yield and damage initiation from zones A to B are denoted in Figure 10 and Figure 11.

To examine the effect of c_A on the initial yield and damage envelopes in a consistent way, the actual ζ value associated with each of the discretizations shown in Figure 4 can be calculated. This is done by rearranging Equation (27),

$$\zeta_{act} = c_f^A \frac{c_A}{c_f} \tag{30}$$

where c_f^A, the average volume fraction in zone A, is calculated for each c_A value by simply averaging the fiber volume fractions of the grid squares in zone A. For example, for $c_A = 0.26$, c_f^A is equal to the average of the shaded entries in Table 1. For $c_A = 0.26$, $\zeta_{act} = 0.35$ ($c_f^A = 0.62$ and $c_f^B = 0.40$); for $c_A = 0.5$, $\zeta_{act} = 0.61$ ($c_f^A = 0.56$ and $c_f^B = 0.36$); for $c_A = 0.74$, $\zeta_{act} = 0.83$ ($c_f^A = 0.51$ and $c_f^B = 0.30$).

The effect of c_A on the predicted composite initial yield and damage envelopes of the carbon/epoxy composite, where $\zeta = \zeta_{act}$, is shown in Figure 12. Clearly, the variation among the envelopes is less than that shown in Figure 9 to Figure 11. This is expected as, for all three cases of $c_A = 0.26$, 0.5, and 0.74, the ζ_{act} value is between the values of ζ used in Figure 9 to Figure 11. However, this also indicates that the choice of c_A used to discretize the microstructure is not critical.

In order to illustrate the effect of material system on the impact of fiber clustering, the initial yield and damage envelopes of an E-glass/epoxy composite have also been examined. The considered isotropic elastic properties of the E-glass fibers are: $E = 73$ GPa and $\nu = 0.22$, while the same epoxy matrix is considered. The mismatch in transverse Young's modulus between the fiber and matrix is known to have a significant effect on the local fields within composites. For the carbon/epoxy composite considered above, this mismatch is $12.4/5.2 = 2.4$, whereas for the glass/epoxy composite, it is $73/5.2 = 14$. Note that the identical carbon/epoxy microstructure (Figure 3) and idealizations into zones (Figure 4) were used.

Figure 13 shows the effect of c_A on the predicted composite initial yield and damage envelopes of the E-glass/epoxy composite, where $\zeta = \zeta_{act}$. Compared to the carbon/epoxy composite (Figure 12), it is clear that the effect of clustering on the initial yield and damage envelopes is much greater in the case of the E-glass/epoxy composite. The E-glass/epoxy's greater mismatch in the fiber-matrix transverse Young's modulus leads to higher stress concentrations due to the presence of clustering, which are manifested in the predicted envelopes. Similarly, there are now some noticeable variations in the envelopes based on the choice of c_A, but, as in the case of the carbon/epoxy composite, this difference is significantly less than the difference between the uniform case and any of the clustered cases.

Initial Yield Envelopes

Initial Damage Envelopes
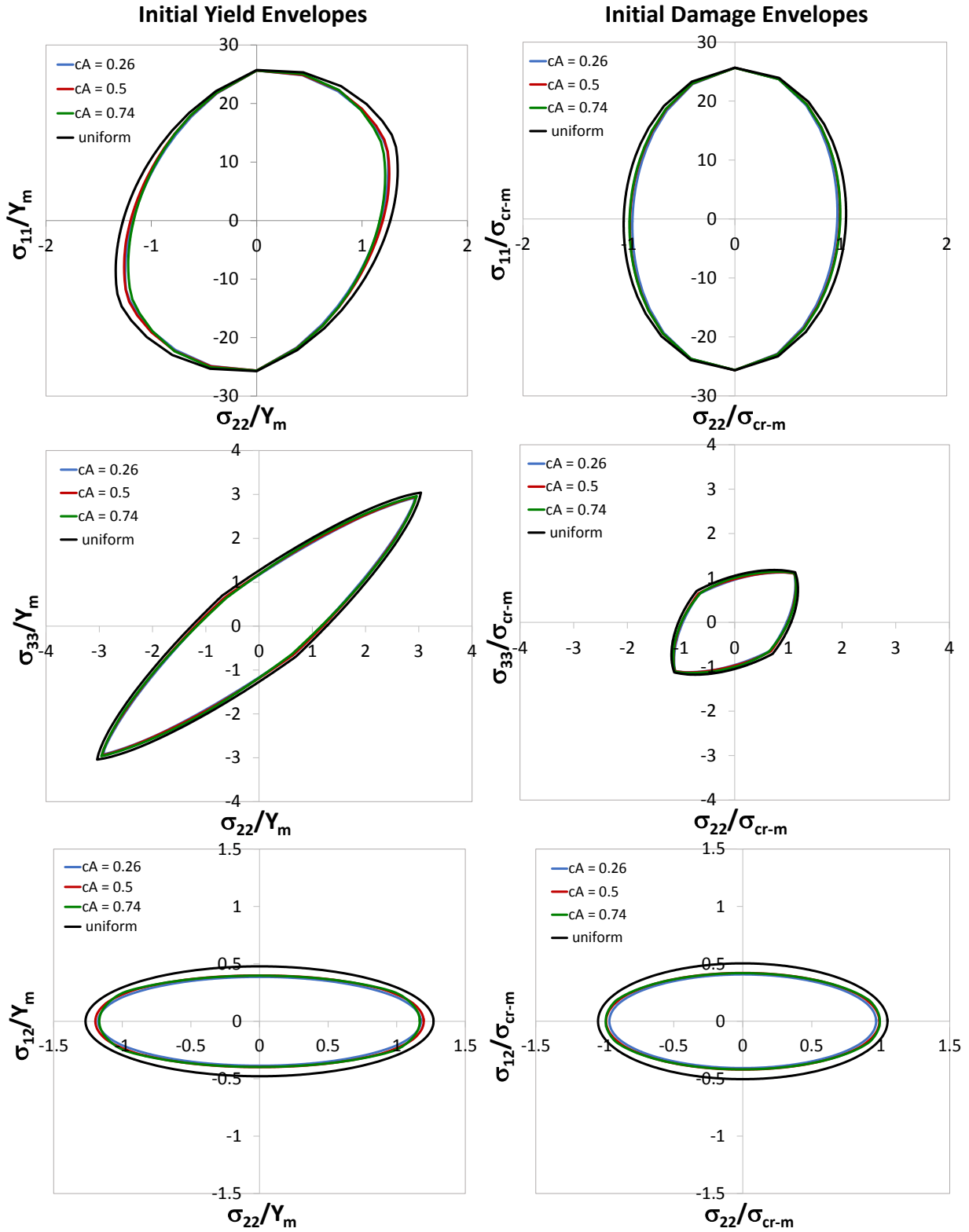
Figure 12.—Comparison of initial yield and damage envelopes for the carbon/epoxy composite, for different values of c_A with $\zeta = \zeta_{act}$.

Initial Yield Envelopes

Initial Damage Envelopes
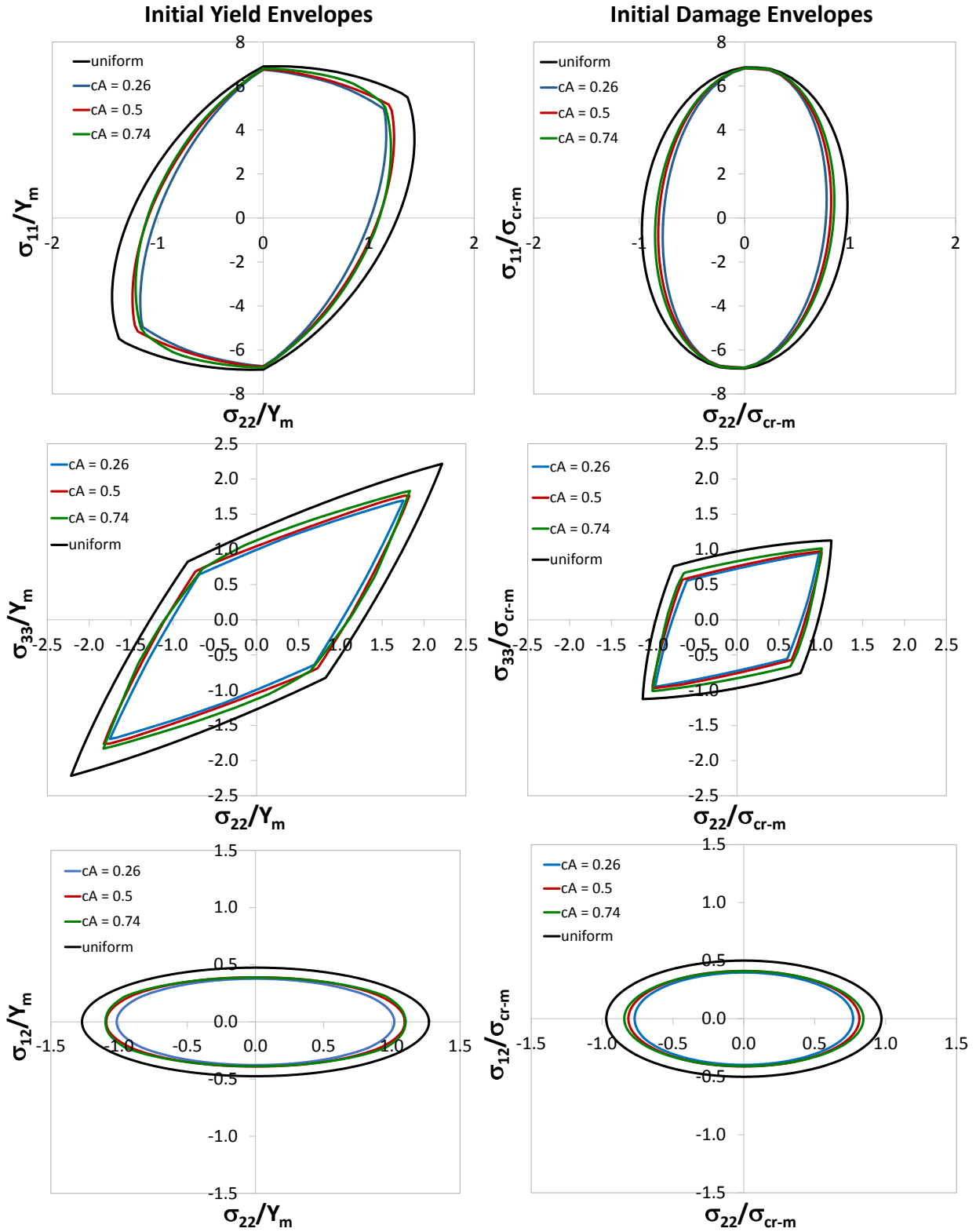
Figure 13.—Comparison of initial yield and damage envelopes for the E-glass/epoxy composite, for different values of c_A with $\zeta = \zeta_{act}$.

Nonlinear Effective Stress-Strain Curves

To examine the effect of fiber clustering on the nonlinear behavior of the composite, the epoxy matrix material response was simulated using the nonlinear elastic Ramberg and Osgood (1943) model. The uniaxial form of the constitutive relation in this model is given by,

$$\varepsilon = \frac{\sigma}{E} + \frac{\sigma_0}{E}\left(\frac{\sigma}{\sigma_0}\right)^n \tag{31}$$

where E is the Young's modulus and σ_0 and n are two material parameters that can be determined by fitting the material nonlinear stress-strain response. A deviatoric multiaxial generalization is given by

$$\varepsilon_{ij} = \frac{1+\nu}{E}\sigma_{ij} - \frac{\nu}{E}\sigma_{kk}\delta_{ij} + \frac{3}{2E}\hat{\sigma}_{ij}\left(\frac{\sigma_{eq}}{\sigma_0}\right)^{n-1} \tag{32}$$

where ν is the Poisson's ratio and σ_{eq} is the equivalent stress (see Eq. (18)).

In the implementation of Equation (32) within the multiscale HFGMC model described above, it is necessary to cast this equation in its incremental form,

$$\Delta\varepsilon_{ij} = S_{ijkl}\,\Delta\sigma_{kl} \tag{33}$$

where S_{ijkl} are the components of the instantaneous compliance tensor, which can be obtained from manipulation of the incremental form of Equation (32). Then, inverting **S**, the local subcell constitutive equation (10), including the Ramberg-Osgood nonlinear effects, is obtained. The remainder of the incremental multiscale HFGMC theory remains the same as presented above.

The nonlinearity of the epoxy material has been modeled herein by choosing two sets of parameters with different degrees of nonlinearity: $\sigma_0 = 158$ MPa, $n = 4$ (from Aboudi, 1991) and $\sigma_0 = 80$ MPa, $n = 15$ (fictional values, resulting in greater nonlinearity). The resulting uniaxial stress-strain curves in simple tension are shown in Figure 14.

The resulting effective transverse stress-strain curves of the composite at the global scale are shown in Figure 15 for the three values of c_A with varying ζ and for both sets of nonlinear parameters. It can be readily observed that the effect of clustering on the C/epoxy composite is greater when more matrix nonlinearity is present. It would be expected that this effect would continue to increase with decreasing matrix instantaneous stiffness. In addition, by comparing the three plots in Figure 15, it can be seen that for $c_A = 0.26$, the curve associated with higher ζ has the greater deviation from the uniform case, whereas for $c_A = 0.74$, the curve associated with lower ζ has the greater deviation from the uniform case. For intermediate value of $c_A = 0.5$, the curves associates with both values of ζ are very similar. As in the case of the initial envelopes, the greatest deviation from the uniform results is always associated with the higher local fiber volume fraction being located in the zone with the lower volume fraction within the global RUC.

Once again, to illustrate the effect of the contrast between the properties of the fibers and the matrix on the impact of fiber clustering, the stress-strain response of the E-glass/epoxy composite has been examined. The more nonlinear epoxy Ramberg-Osgood parameters, $\sigma_0 = 80$ MPa, $n = 15$, were employed in the following simulations.
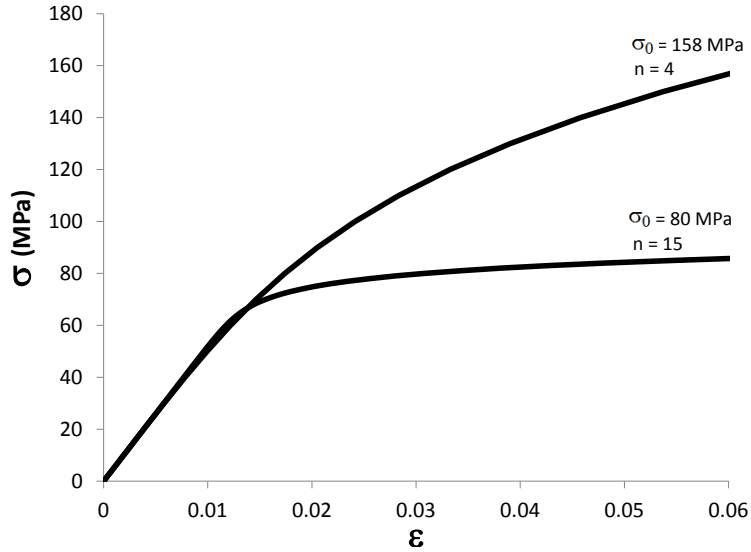
Figure 14.—Uniaxial stress-strain curves of the nonlinear epoxy in simple tension, as represented by the Ramberg-Osgood model with E = 5.2 GPa, ν = 0.35 and the two sets of nonlinear parameters indicated.
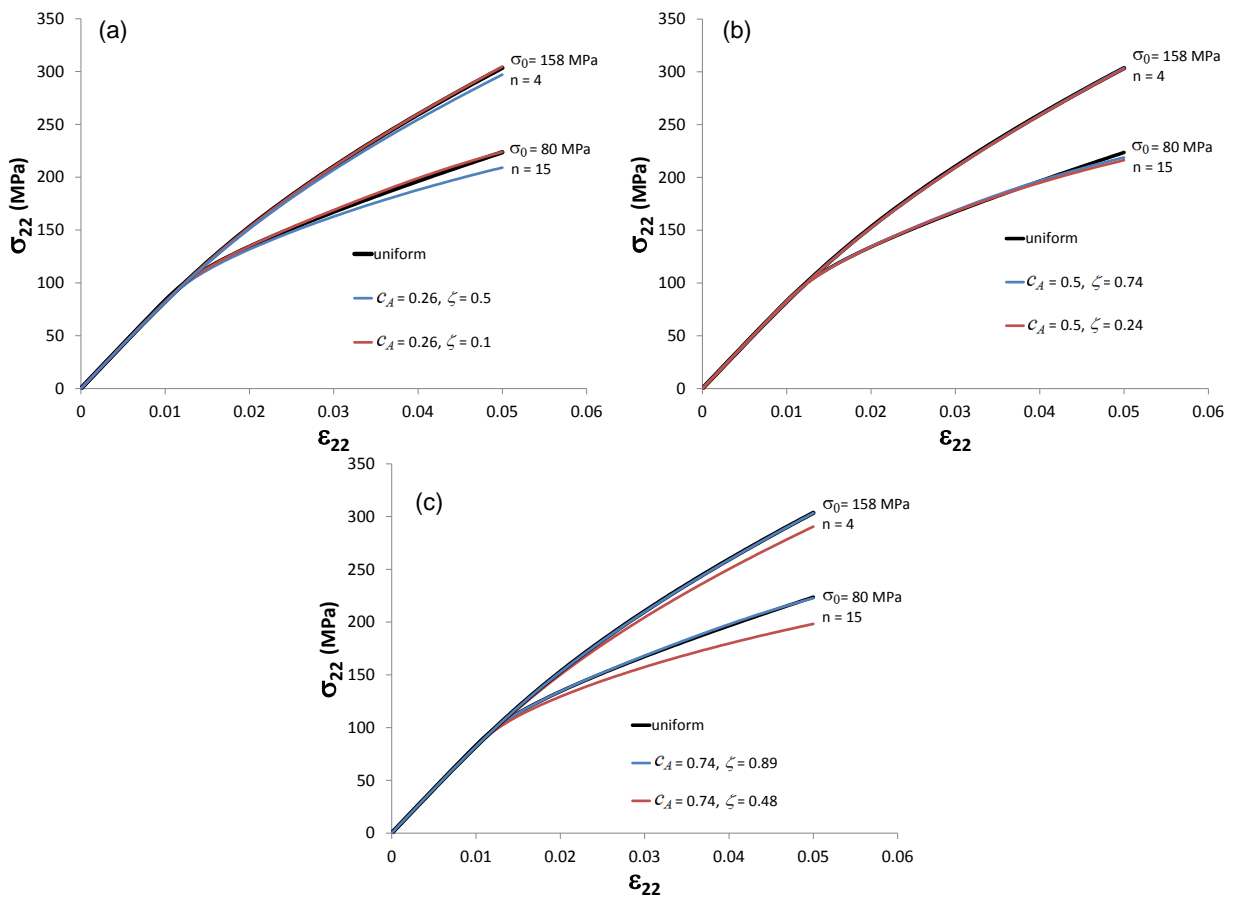
Figure 15.—Effective transverse response of the C/epoxy composite using two sets on nonlinear parameters for the matrix. (a) c_A = 0.26, (a) c_A = 0.5, (a) c_A = 0.74.
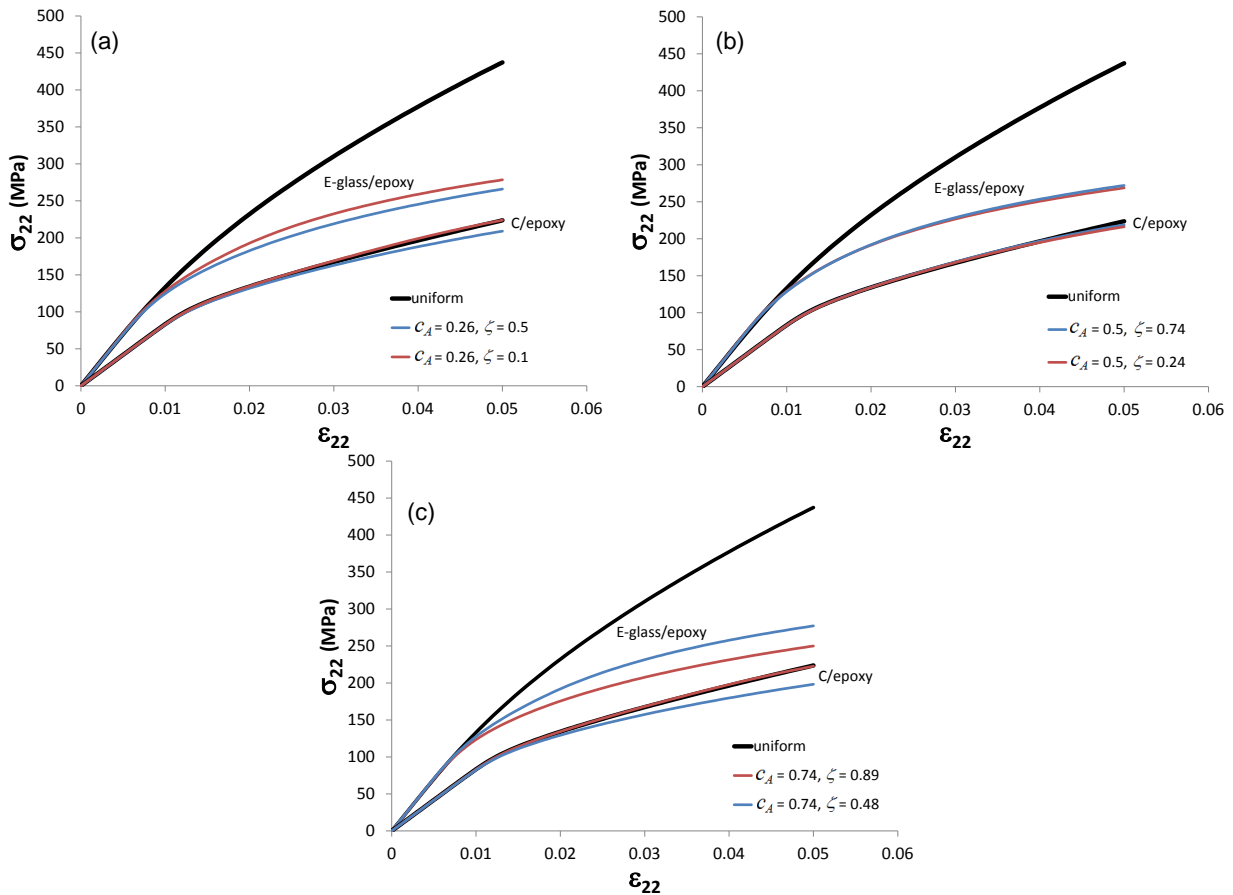
Figure 16.—Effective transverse response of the E-glass/epoxy composite compared with the C/epoxy composite. (a) $c_A = 0.26$, (a) $c_A = 0.5$, (a) $c_A = 0.74$.

The results of the transverse tensile simulations of the E-glass/epoxy composite are compared to the C/epoxy composite in Figure 16. Obviously, because the E-glass fiber has a higher transverse stiffness, the E-glass/epoxy composite also has a higher effective transverse stiffness. In addition, the higher transverse mismatch in fiber-matrix properties results in a much greater influence of fiber clustering on the effective transverse response. Otherwise, the trend with respect to the parameter ζ is the same in the E-glass/epoxy composite as in the C/epoxy system.

Alternative Microstructure

To investigate the influence of the assumed global microstructure, an alternative global microstructure, taken from a different specimen of the same type of composite, was considered. The micrograph is shown in Figure 17. As before, a square grid was placed over the micrograph and the local fiber volume fraction within each square was determined via image pixel analysis. Because the aspect ratio of the present micrograph shown in Figure 17 is different than the previous micrograph shown in Figure 3, a grid of 10 x 24 squares was required. The overall fiber volume fraction, c_f, determined via image pixel analysis of the alternative micrograph is 0.452. A comparison of Figure 5 and Figure 18 indicates that the two global RUCs are quite different, with the latter having the majority of zone A located in the right half of the RUC.
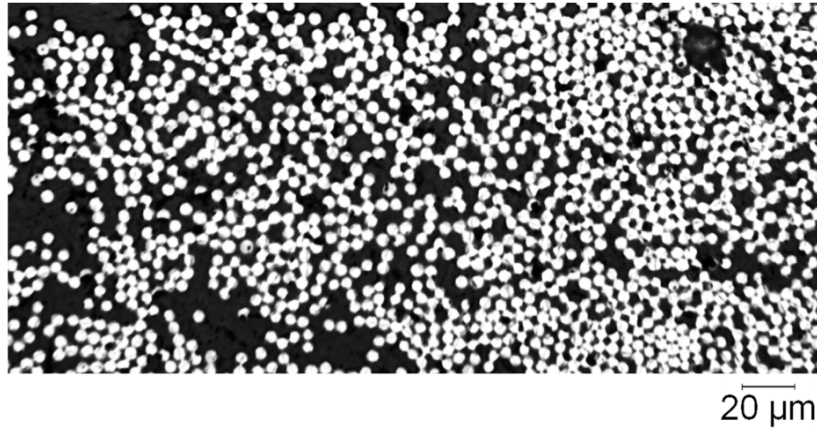
Figure 17.—Alternative micrograph from a 0° ply in an IM7/MTM-45 carbon/epoxy composite. The overall fiber volume fraction, based on image pixel analysis, is 0.452.

$c_f^A = 0.89$ $c_f^B = 0.30$
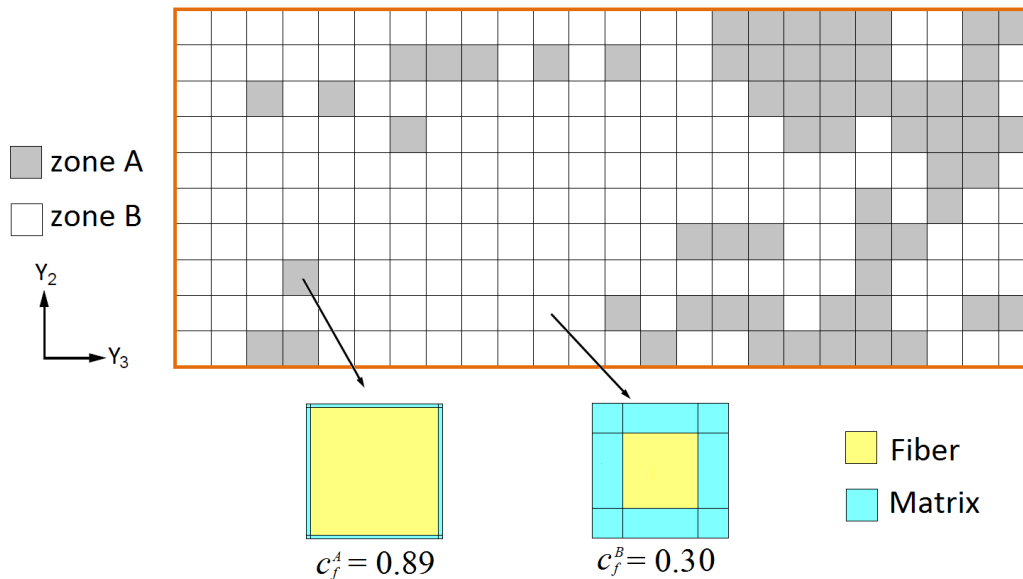
Figure 18.—Multiscale material distribution for $c_A = 0.25$ with $\zeta = 0.5$, for the alternative composite micrograph shown in Figure 17.

In order to compare to the previous results, a $c_A = 0.25$ was obtained using a fiber volume fraction cutoff of 0.55. Note that it was not possible to match the previous $c_A = 0.26$ exactly. The resulting global scale RUC is shown in Figure 18, along with the local RUCs and local fiber volume fractions corresponding to $\zeta = 0.5$.

A comparison of the initial yield and damage envelopes of the original microstructure with the present alternative microstructure is shown in Figure 19. These comparisons are shown for $c_A = 0.25$ or 0.26 and $\zeta = 0.5$. As can be seen, although the micrographs used to generate the global RUCs are quite different, the predicted initial envelopes under normal loadings are nearly identical. However, for the axial shear case, the envelopes show variation under significant shear loading. Thus because of this variation in the shear responses, it is not possible to claim that the clustering is fully characterized by the parameters c_A and ζ. Rather, the chosen global scale microstructure can also have an effect. It should be noted, however, that, since only two particular microstructures were considered, the sample size is in no way statistically representative. Similarly, no assessment has been made of the statistical relevance of two specific microstructures considered in terms of their size and number of fibers included.

A comparison between the global transverse stress-strain curves obtained from the original microstructure and the present alternative microstructure is shown in Figure 20, in which $c_A = 0.25$ or 0.26 and $\zeta = 0.5$. It can be observed that the two responses are again quite similar.

Initial Yield Envelopes   Initial Damage Envelopes
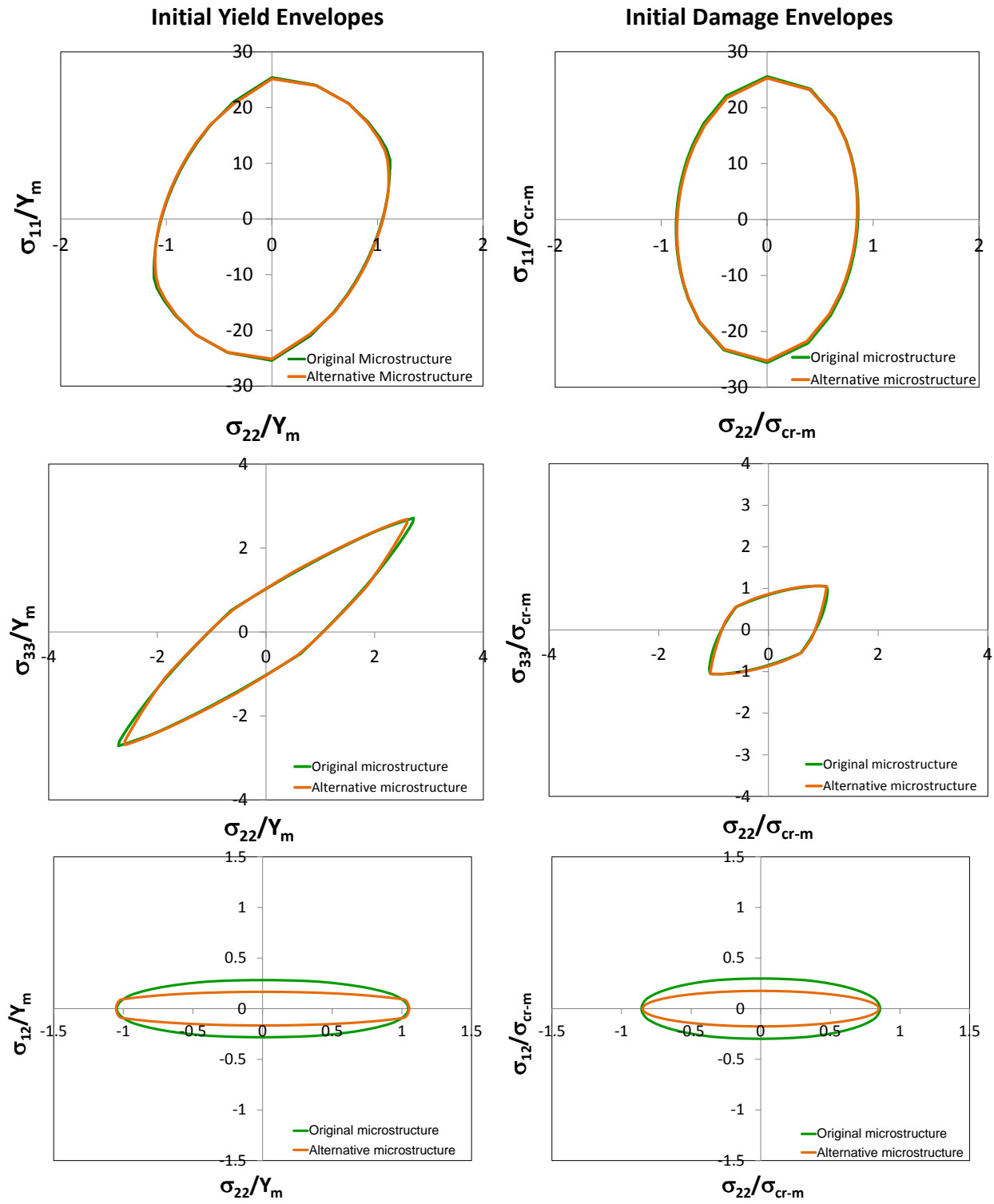
Figure 19.—Comparison of initial yield and damage envelopes for $c_A = 0.26$ and $\zeta = 0.5$ from the original (Figure 5) and alternative (Figure 18) microstructures.
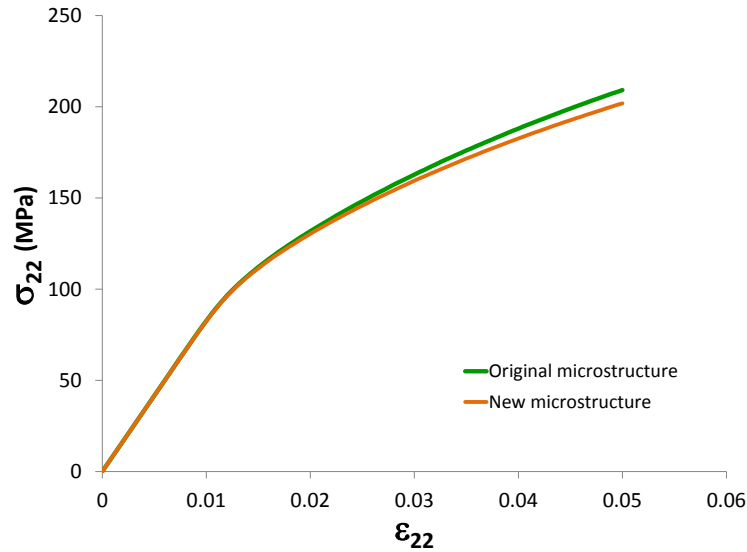
Figure 20.—Comparison of the effective transverse response of the C/epoxy composite for the original and alternative microstructures with $c_A = 0.26$ and $\zeta = 0.5$. The nonlinear epoxy parameters, $\sigma_0 = 80$ MPa, $n = 15$, were employed.

Conclusions

A multiscale micromechanical approach has been developed for the prediction of the behavior of composites exhibiting fiber clustering. The method is able to predict not only effective composite properties, but also initial yield and damage envelopes, as well as the nonlinear stress-strain response of the composite, due to the availability of local fields. This is possible because this approach is based on the establishment of the concentration tensors on the local and global scales. Fiber clustering is characterized by two nondimensional parameters, which measure the extent and density of the fiber clusters, along with a global RUC determined from actual composite micrographs. This methodology was applied to carbon/epoxy and E-glass/epoxy composites. It has been shown that fiber clustering results in a decrease in the sizes of the initial yield and damage surfaces as compared to the uniformly distributed case. The effect is greater in the case of E-glass/epoxy compared to the baseline carbon/epoxy due to greater mismatch in the fiber-matrix transverse Young's modulus mismatch in the case of the E-glass/epoxy. In addition, transverse stress-strain simulations indicated that the effect of fiber clustering increases with increasing fiber-matrix property mismatch and with increasing nonlinearity of the matrix.

The present method, which can consider three dimensional composite microstructures, could also be applied to the simulation of nanocomposites, whose low volume fractions tend to result in significant amounts of clustering. Ceramic matrix composites, which typically have brittle matrices and lower fiber volume fractions than polymer matrix composites, would also be expected to exhibit significant effects of fiber clustering. Further, since HFGMC has been formulated to include inelasticity, fiber-matrix debonding (Aboudi et al., 2013), fiber misalignment (Bednarcyk et al., 2014), and progressive damage (Bednarcyk et al., 2010; Pineda et al., 2013), these effects can be incorporated at the local scale in the present multiscale implementation to determine the impact of their combination with fiber clustering on the composite behavior.

References

Abhilash, A.S., Joshi, S.P., Mukherjee, A., and Mishnaevsky Jr., L. (2011) Micromechanics of diffusion-induced damage evolution in reinforced polymers. Comp. Sci. Tech. 71, 333-342.

Aboudi, J., Arnold, S.M., and Bednarcyk, B.A. (2013) Micromechanics of Composite Materials A Generalized Multiscale Approach, Elsevier, New York.

Aboudi, J. (1991) Mechanics of Composite Materials A Unified Micromechanical Approach, Elsevier, New York.

Acton, K. and Graham-Brady, L. (2010) Elasto-plastic mesoscale homogenization of composite materials. J. Engr. Mech. 136, 613-624.

Al-Ostaz, A. Diwakar, A., and Alzebdeh, K.I. (2007) Statistical model for characterizing random microstructure of inclusion-matrix composites. J. Mater. Sci. 42, 7016-7030.

Baxter, S.C., Graham-Brady, L.L., Xu, X.F. (2005) Modeling the effects of material nonlinearity using moving window micromechanics. Int. J. Nonlinear Mech. 40, 351-359.

Baxter, S.C. and Graham, L.L. (2000) Characterization of random composite materials using the moving-window generalized method of cells technique. J. Engr. Mech. 126, 389-397.

Bednarcyk, B.A., Aboudi, J, and Arnold, S.M. (2010) Micromechanics modeling of composites subjected to multiaxial progressive damage in the constituents. AIAA J. 48, 1367-1378.

Bednarcyk, B.A., Aboudi, J., and Arnold, S.M. (2014) The effect of general statistical fiber misalignment on damage initiation in composites. *Composites: Part B*, 66, 97-108.

Bednarcyk, B.A., Mital, S.K., Pineda, E.J., and Arnold, S.M. (2015) Multiscale Modeling of Ceramic Matrix Composites, 56th AIAA/ASME/ASCE/AHS/ASC Structures, Structural Dynamics, and Materials Conference, January 5-9, Kissimmee, FL.

Ghosh, S., Nowak, Z., and Lee, K. (1997) Quantitative characterization and modeling of composite microstructures by Voronoi cells. Acta Mater. 45, 2215-2234.

Graham-Brady, L.L., Siragy, E.F., Baxter, S.C. (2003) Analysis of heterogeneous composite materials using moving-window techniques. J. Engr. Mech. 129, 1054-1064.

Guild, F.J. and Summerscales, J. (1993) Microstructural image analysis applied to fibre composite materials: a review. Composites 24, 383-393.

Lemaitre, J. (2001) Handbook of Materials Behavior Models, Elsevier, New York.

Lemaitre, J. and Chaboche, J.L. (1990) Mechanics of Solid Materials, Cambridge University Press, Cambridge.

Liu, K.C. and Arnold, S.M. (2013) Influence of scale specific features on the progressive damage of woven ceramic matrix composites (CMCs). CMC 35, 35-65.

Liu, K.C., Chattopadhyay, A., Bednarcyk, B.A., Arnold, S.M. (2011) Efficient multiscale modeling framework for triaxially braided composites using generalized method of cells. Journal of Aerospace Engineering 42, 162-170.

Melro, A.R., Camanho, P.P., and Pinho, S.T. (2008) Generation of random distribution of fibres in long-fibre reinforced composites. Comp. Sci. Tech. 68, 2092-2101.

Pindera, M.-J. and Aboudi, J. (1988) Micromechanical analysis of yielding of metal matrix composites. Int. J. Plasticity 4, 195-214.

Pineda, E.J., Bednarcyk, B.A., Waas, A.M., and Arnold, S.M. (2013) Progressive failure of a unidirectional fiber-reinforced composite using the method of cells: discretization objective computational results. Int. J. Solids Struct. 50, 1203-1216.

Pyrz, R. (1994) Quantitative description of the microstructure of composites. Part I: Morphology of unidirectional composite systems. Comp. Sci. Tech. 50, 197-208.

Ramberg, W. and Osgood, W. R. (1943) Description of stress-strain curves by three parameters. *Technical Note No. 902*, National Advisory Committee For Aeronautics, Washington DC.

Romanov, V., Lomov, S.V., Swolfs, Y., Orlova, S., Gorbatikh, L., and Verpoest, I. (2013) Statistical analysis of real and simulated fibre arrangements in unidirectional composites. Comp. Sci. Tech. 87, 126-134.

Scalon, J.D., Fieller, N.R.J., Stillman, E.C., and Atkinson, H.V. (2003) Spatial pattern analysis of second-phase particles in composite materials. Mater. Sci. Engr. A356, 245-257.

Shaffer, M.S.P. and Windle, A.H. (1999) Fabrication and characterization of carbon nanotube/poly(vinyl alcohol) composites. Adv. Mater. 11, 937-941.

Shi, D.-L., Feng, X.-Q., Huang, Y.Y., Hwang, K.-C., and Gao, H. (2004) The effect of nanotube waviness and agglomeration on the elastic properties of carbon nanotube-reinforced composites. J. Eng. Mater. Tech. 126, 250-257.

Sorensen, B.F. and Talreja, R. (1993) Effects of nonuniformity of fiber distribution on the thermally-induced residual stresses and cracking in ceramic matrix composites. Mech. Mater. 16, 351-363.

Vaughan, T.J. and McCarthy, C.T. (2010) A combined experimental-numerical approach for generating statistically equivalent fiber distributions for high strength laminated composite materials. Comp. Sci. Tech. 70, 291-297.

Vigolo, B., Penicaud, A.P., Couloun, C., Sauder, S., Pailler, R., Journet, C., Bernier, P., and Poulin, P. (2000) Macroscopic fibers and ribbons of oriented carbon nanotubes. Science 290, 1331-1334.

Wilding, S.E. and Fullwood, D.T. (2011) Clustering metrics for two-phase composites. Comput. Mater. Sci. 50, 2262-2272.

Wongsto, A. and Li, S. (2005) Micromechanical FE analysis of UD fibre-reinforced composites with fibres distributed at random over the transverse cross-section. Composites A 36, 1246-1266.

Yang, S., Gokhale, A.M., and Shan, Z. (2000) Utility of microstructure modeling for simulation of micro-mechanical response of composites containing non-uniformly distributed fibers. Acta mater. 48, 2307-2322.

Yang, S. Tewari, A., and Gokhale, A.M. (1997) Modeling of non-uniform spatial arrangement of fibers in ceramic matrix composites. Acta mater. 45, 3059-3069.

Zangenberg, J., Larsen, J.B., Østergaard, R.C., and Brøndsted, P. (2012) Methodology for characterisation of glass fibre composite architecture. Plastics, Rubber and Composites 41, 187-193.

Zeman, J. and Sejnoha, M. (2001) Numerical evaluation of effective elastic properties of graphite fiber tow impregnated by polymer matrix. J. Mech. Phys. Sol. 49, 69-90.